
INFINITE SELF-ATTENTION

PREPRINT — FEBRUARY 2026

Giorgio Roffo 
 Equixly API Security
 giorgio.roffo@equixly.com

ABSTRACT

The quadratic cost of softmax attention limits Transformer scalability in high-resolution vision. We introduce *Infinite Self-Attention* (InfSA), a spectral reformulation that treats each attention layer as a diffusion step on a content-adaptive token graph, accumulating multi-hop interactions through a discounted Neumann series over attention matrices. This formulation connects self-attention to classical graph centrality measures—Katz, PageRank, and eigenvector centrality—yielding interpretable and structurally grounded token weighting. We further show that this Neumann kernel coincides with the fundamental matrix of an absorbing Markov chain [1, 2], linking each token’s centrality score to its expected number of random-walk visits before absorption. Building on this, we propose *Linear-InfSA*, an $\mathcal{O}(N)$ variant that approximates the principal eigenvector of the implicit attention operator without forming the $N \times N$ matrix. It maintains an auxiliary state of fixed size $\mathcal{O}(d_h)$ —where d_h is the per-head dimension, independent of the sequence length N —is drop-in compatible with standard Vision Transformers, and supports stable forward and backward passes at 4096^2 resolution and inference at 9216^2 ($\sim 332k$ tokens). Integrated into a 4-layer ViT with 53.5M parameters and 59 GFLOPs at 224^2 , Linear-InfSA achieves 84.7% top-1 on ImageNet-1K, a +3.2 pp purely architectural gain over a standard 4-layer ViT baseline (81.5%) trained with an identical recipe. On ImageNet-V2, all InfViT variants surpass every compared baseline (up to 79.8% vs. 76.8% for the best prior method), indicating robust generalization under distribution shift. Attention quality evaluations confirm semantically grounded maps: MoRF-AOC reaches 76.0% and bounding-box PR-AUC 76.1%, versus 42.6% and 56.2% respectively for softmax ViT. In scalability benchmarks on an A100 40 GB GPU, Linear-InfViT delivers 231 img/s at 0.87 J/img—a $13\times$ improvement in both throughput and energy over a standard ViT of equal depth—and is the only tested model to complete 9216^2 inference without running out of memory. The linear approximation faithfully recovers the dominant eigenvector of the full quadratic operator (cosine similarity 0.985). Code and pretrained weights are available at <https://github.com/giorgioroffo/infinite-self-attention>.

Keywords Graph diffusion attention · Absorbing Markov chains · Linear-complexity Vision Transformers · Eigenvector centrality · Interpretable attention maps

1 Introduction

Transformer architectures underpin modern vision [3–5] and language models [6–8], yet their quadratic attention cost limits scalability in high-resolution and long-context settings [9, 10]. This has motivated numerous efficient attention mechanisms [11–14]. This computational bottleneck also carries environmental cost: data-centre consumption is projected to nearly double by 2030 [15, 16], and quadratic attention dominates Transformer energy budgets [17].

Despite progress, most efficient variants approximate or sparsify the attention matrix without a principled model of token interaction. Standard Transformers aggregate dependencies implicitly across stacked layers, offering limited control over multi-hop influence or interpretability. Empirical analyses further show that attention weights may highlight diffuse or semantically irrelevant regions [18, 19]. Graph-theoretic formulations offer a more structured perspective: diffusion processes quantify node influence through centrality measures such as Katz [20], PageRank [21, 22], and eigenvector centrality [23], enabling explicit multi-hop reasoning and structural interpretability—yet such principles remain underexplored within Transformer architectures. Notably, the connection between infinite-path aggregation on weighted graphs and absorbing Markov chains was established by Roffo *et al.* [1, 24], who showed that the funda-

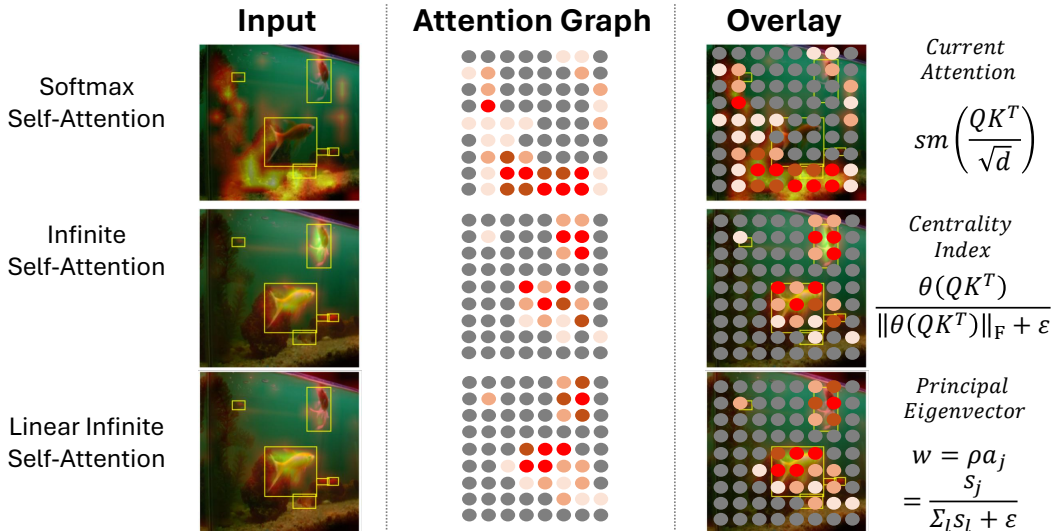


Figure 1: **Comparison of attention graphs.** Visualization of ViT-L/16 attention maps on ImageNet. Softmax attention distributes focus across background regions, while InfSA variants produce sharper, object-aligned activations.

mental matrix of a substochastic random walk yields the same Neumann kernel $N = (I - \gamma A)^{-1}$ used for centrality scoring, with entry N_{ij} equal to the expected number of visits to node j before absorption when starting from node i .

We introduce *Infinite Self-Attention (InfSA)*, a spectral diffusion view of attention that aggregates information across layers through a truncated Neumann-series construction, akin to infinite-path kernels used in Katz/PageRank scoring [1, 24]. The same Neumann kernel admits an absorbing Markov chain interpretation [1, 2]: tokens are transient states of a random walk on the attention graph, and their centrality scores correspond to expected visit counts before diffusion terminates. We also develop *Linear-InfSA*, a scalable $\mathcal{O}(N)$ variant that approximates dominant attention directions via the $A^{k \rightarrow \infty}$ eigenvector limit (see Fig. 1). Integrated into Vision Transformers, InfSA delivers strong ImageNet-1K/V2 accuracy, sharper and more localized attention maps, and stable scaling to 4K–9K inputs; full derivations and extended analyses are provided in subsequent sections.

Contributions.

- We connect attention propagation to eigenvector dynamics and nonlinear Perron–Frobenius theory, offering a principled view of global token influence.
- We introduce *InfSA*, a spectral generalization of self-attention via graph diffusion and Neumann-series path integrals, and show that the resulting attention graph admits an absorbing Markov chain interpretation in which token centrality equals expected random-walk visits before absorption.
- We propose *Linear-InfSA*, an $\mathcal{O}(N)$ approximation that avoids attention matrix construction, with a fixed-size $\mathcal{O}(d)$ auxiliary state independent of N , enabling stable scaling to high resolutions.
- Experiments on vision tasks illustrate interpretability, robustness, and scalability; InfSA establishes a conceptual foundation for efficient AI architectures.

The rest of the paper is organized as follows: Sec. 2 reviews related work on efficient attention, graph centrality, and state-space models; Sec. 3 derives Pure InfSA from the path-integral perspective and its absorbing Markov chain interpretation, then introduces Linear-InfSA; Sec. 4 evaluates scalability, attention quality, classification performance, ablations, eigenvector alignment, and qualitative analysis; Sec. 5 discusses scope and future directions; Sec. 6 concludes.

2 Related Work

Efficient Attention. The quadratic cost of softmax attention has driven sustained research into sub-quadratic alternatives, which can be grouped by asymptotic complexity.

Table 1: **Asymptotic complexity of attention mechanisms.** N : sequence length; d : head dimension; k/M : fixed rank / agent count. “Attn. state” refers to the per-head auxiliary memory for attention computation, excluding input/output activations which are $\mathcal{O}(Nd)$ for all methods.

Method	Time	Attn. state	Tier
Softmax / FlashAttn [13]	$\mathcal{O}(N^2d)$	$\mathcal{O}(N^2) / \mathcal{O}(N)$	Quadratic
Performer [10]	$\mathcal{O}(Nd^2)$	$\mathcal{O}(d^2)$	Feature-map
FLatten [25]	$\mathcal{O}(Nd^2)$	$\mathcal{O}(d^2)$	Feature-map
MLLA [26]	$\mathcal{O}(Nd^2)$	$\mathcal{O}(d^2)$	Feature-map
Linformer [11]	$\mathcal{O}(Nkd)$	$\mathcal{O}(kd)$	Projection
SOFT [27]	$\mathcal{O}(Nd)$	$\mathcal{O}(d)$	Projection
Agent Attn [28]	$\mathcal{O}(NMd)$	$\mathcal{O}(Md)$	Projection
Fastformer [29]	$\mathcal{O}(Nd)$	$\mathcal{O}(d)$	Projection
Linear-InfSA (Ours)	$\mathcal{O}(N)$	$\mathcal{O}(d)$	Linear

$\mathcal{O}(Nd^2)$ methods replace the $N \times N$ attention matrix with a product of smaller feature maps. Performer [10] approximates softmax via random Fourier features, resulting in $\mathcal{O}(Nd^2)$ time and $\mathcal{O}(Nd)$ memory, where d is the projection dimension. FLatten [25] recovers the expressiveness lost in focused linear attention through a rank-restoration mechanism whose cost also scales as $\mathcal{O}(Nd^2)$. MLLA [26] recasts Mamba-style selective gating as linear attention, retaining an $\mathcal{O}(Nd^2)$ bottleneck from the outer-product state update. For all three, the quadratic dependence on d means that at standard head dimensions ($d_h=64$, sometimes even $d_h=128$) these methods remain noticeably slower than truly linear alternatives when N is large.

$\mathcal{O}(Nd)$ methods project keys or queries to a fixed rank that does not depend on N . Linformer [11] projects keys and values to a fixed k -dimensional subspace, achieving $\mathcal{O}(Nk)$ cost; k is typically set to $\mathcal{O}(d)$. SOFT [27] applies softmax-free Gaussian kernels to achieve linear complexity without random features. Agent Attention [28] bridges softmax and linear attention through a small set of learnable agent tokens that aggregate global context, giving $\mathcal{O}(NMd)$ cost where $M \ll N$ is the fixed number of agents. Fastformer [29] replaces pairwise attention with additive pooling, which can be seen as an extreme rank-1 projection, achieving $\mathcal{O}(Nd)$ at the cost of expressiveness. While these methods scale linearly in N , they retain a multiplicative dependence on the head dimension d , which affects wall-clock performance in multi-head architectures with large d .

IO-optimized exact attention. FlashAttention [13, 30, 31] implements exact softmax attention through tiled, fused kernels that are aware of the GPU memory hierarchy. This eliminates the $\mathcal{O}(N^2)$ memory wall but retains $\mathcal{O}(N^2)$ compute: the FLOPs are unchanged, making 300k+ token sequences prohibitively slow even though they fit in memory. FlashAttention is therefore complementary to—not a replacement for—truly sub-quadratic methods.

$\mathcal{O}(N)$: *Linear-InfSA.* Our Linear-InfSA computes a global context vector of fixed size $\mathcal{O}(d_h)$ —independent of N —and broadcasts it back to all tokens. The per-token cost is $\mathcal{O}(1)$ in terms of N , giving an overall $\mathcal{O}(N)$ complexity that is independent of d_h in the attention computation itself. This places Linear-InfSA strictly below all of the above tiers: it avoids both the $\mathcal{O}(N^2)$ pairwise computation of softmax attention, the $\mathcal{O}(Nd^2)$ feature-map cost of kernel-based methods, and the $\mathcal{O}(Nd)$ projection cost of rank-reduction methods. Table 1 summarizes the complexity landscape.

Graph Centrality, Markov Chains, and Feature Selection. The idea of interpreting pairwise interactions as a graph and deriving node importance from structural properties has a long history. Bonacich [23, 32] formalized eigenvector centrality for social networks, showing that a node’s importance is proportional to the sum of the importances of its neighbors—the dominant eigenvector of the adjacency matrix. Katz [20] proposed a related index that sums attenuated walks of all lengths, leading to the Neumann series $(I - \gamma A)^{-1}$; Page *et al.* [21, 22, 33] adapted this principle to the web graph as PageRank.

In the context of machine learning, Roffo *et al.* [24] introduced *Infinite Feature Selection* (Inf-FS) at ICCV 2015, recasting feature selection as a weighted-graph ranking problem. Each feature becomes a node, pairwise relations define edges, and the total importance of a feature is obtained by summing all paths of all lengths on this graph—the matrix power series $\sum_{t \geq 1} A^t$. To ensure convergence, the series is closed in closed form via the Neumann kernel $(I - rA)^{-1} - I$, where $r \geq 1/\rho(A)$. This was the first work to show that infinite-path aggregation on an affinity graph can be computed in closed form and used for unsupervised feature ranking.

The theory was substantially extended in Roffo *et al.* [1] (IEEE TPAMI, 2021), which established that the same Neumann kernel coincides with the *fundamental matrix* $N = (I - Q)^{-1}$ of an absorbing Markov chain, where Q is the substochastic transition matrix of the transient (feature) states. Entry N_{ij} equals the expected number of visits to feature j before absorption, starting from feature i . This Markov-chain interpretation provides a probabilistic

semantics for the algebraic path-integral: feature centrality is literally the expected diffusion footprint of a random walker on the feature graph.

Roffo and Melzi [34] further connected feature ranking to eigenvector centrality in a workshop paper at ECML-PKDD 2016, observing that the dominant eigenvector of the affinity matrix assigns to each feature a centrality proportional to its recursive influence over all other features. This eigenvector perspective was formalized and experimentally validated in Roffo *et al.* [35], who showed that eigenvector-centrality-based ranking is robust, parameter-free (no discount γ), and competitive with the full Neumann-series approach for large feature sets.

InfSA directly inherits these foundations: we replace features with tokens, the feature-affinity matrix with the attention matrix, and the centrality ranking with token-level importance that modulates the value aggregation in each Transformer layer. Pure InfSA uses the full Neumann-series path integral; Linear-InfSA uses the eigenvector-centrality limit ($v = \lim_{k \rightarrow \infty} A^k x_0 / \|A^k x_0\|_1$), directly inspired by the eigenvector-centrality approach of [34, 35]. This connection is not merely conceptual: the eigenvector alignment study in Sec. 4.5 shows that the Linear-InfSA weights achieve cosine similarity 0.985 with the true Perron eigenvector, empirically validating the link.

Attention as a Markov Chain: InfSA vs. TokenRank. TokenRank [36] independently interprets attention as a Markov chain but computes the *stationary distribution* of a *closed* (ergodic) chain—each token’s score is its steady-state visitation probability. InfSA instead computes the *fundamental matrix* $N = (I - \gamma \hat{A})^{-1}$ of an *absorbing* chain, encoding *expected visit counts* rather than steady-state probabilities. The absorbing formulation has two advantages: (i) the discount factor γ provides explicit control over the effective diffusion depth, and (ii) the expected-visits interpretation assigns independent importance scores to each token pair, whereas a stationary distribution only provides a single scalar per token. Practically, InfSA operates as a drop-in attention replacement inside each Transformer layer, while TokenRank is a post-hoc analysis tool applied to existing attention maps.

Attention Interpretability. Attention rollout [18] propagates raw attention weights across layers; gradient-weighted attention flow [19] combines attention with gradient relevance; perturbation-based saliency [37] and MoRF/LeRF evaluation [38] assess faithfulness by progressively masking input regions. These are diagnostic tools applied *post hoc* to frozen attention maps. In contrast, InfSA embeds centrality directly into the attention mechanism itself, so the derived importance map is both the model’s computational routing *and* its explanation—unifying attention, diffusion, and attribution in a single forward pass.

State-Space and Convolution Models. SSMs such as Mamba [39] and RWKV [40], along with vision adaptations MambaVision [41] and HyenaPixel [42], achieve sub-quadratic modeling via recurrence or long convolutions. These models process tokens sequentially through a hidden state, leveraging hardware-aware scan operators for efficiency. However, they do not derive token importance from graph centrality and lack the multi-hop path-integral interpretation that gives InfSA its interpretability properties. InfSA’s spectral formulation is complementary: it could in principle be layered onto SSM architectures to provide centrality-based token weighting, an avenue we leave for future work.

3 Infinite Self-Attention (InfSA)

Infinite Self-Attention (InfSA) generalizes Transformer self-attention [3] by modeling *multi-hop dependencies* through a spectral, path-based interpretation of token interactions, inspired by Infinite Feature Selection (Inf-FS) [1, 24]. This connects attention to classical *graph diffusion* and *ranking*—Katz, PageRank [20, 21]—and to recent spectral views of attention [1, 43–45]. We derive a layer-wise formulation compatible with standard Transformer blocks and introduce *Linear-InfSA*, a scalable $\mathcal{O}(N)$ variant that bypasses the $N \times N$ attention matrix while preserving the ViT residual structure [3].

3.1 Attention Graphs

We interpret self-attention [3, 6] as a diffusion process on a fully connected, content-adaptive graph $\mathcal{G} = (\mathcal{V}, \mathcal{E})$ where each token is a node and each edge (i, j) has weight $A_{ij} \geq 0$ derived from attention scores. Let $A \in \mathbb{R}^{N \times N}$ denote the attention matrix and $V \in \mathbb{R}^{N \times d}$ the value matrix. The self-attention update is a diffusion step:

$$Y = AV, \tag{1}$$

where each output token aggregates values from all others, weighted by attention [46, 47]. When A is row-stochastic ($A\mathbf{1} = \mathbf{1}$), this is the random-walk operator on \mathcal{G} [48]. Viewing A as an affinity matrix connects attention to centrality measures—PageRank [22], Katz [20], eigenvector centrality—and to Inf-FS [1, 24], which ranks features by structural importance on weighted graphs (see Fig. 1).

3.2 Infinite Self-Attention (InfSA): Path Integrals on the Attention Graph

We extend the attention graph perspective by proposing *Infinite Self-Attention* (InfSA)¹, a formulation inspired by the infinite path integration approach introduced by Roffo *et al.* [1, 24]. That approach ranks features by aggregating the weights of *all* paths on a feature-affinity graph, summing matrix powers $A + A^2 + \dots$ and closing the series via $(I - rA)^{-1} - I$. We map this construction onto self-attention: tokens replace features, the attention matrix replaces the feature-affinity matrix, and the resulting infinite-path scores become token centralities.

Paths on the token graph. Let $\pi = (v_0=i, v_1, \dots, v_{t-1}, v_t=j)$ denote a path of length t from token i to token j in the attention graph \mathcal{G} . The *path weight* is the product of attention weights along edges:

$$w(\pi) = \prod_{k=0}^{t-1} A(v_k, v_{k+1}). \quad (2)$$

This product measures the cumulative affinity along the path: it is high when all consecutive tokens are mutually relevant.

Aggregation over all paths of fixed length. Let \mathbb{P}_{ij}^t be the set of all paths of length t from i to j . The total contribution of length- t paths is

$$R_t(i, j) = \sum_{\pi \in \mathbb{P}_{ij}^t} w(\pi). \quad (3)$$

By standard matrix algebra [49], this equals the (i, j) -entry of the t -th power of A :

$$R_t = A^t. \quad (4)$$

In other words, $A^t(i, j)$ aggregates the contributions of *all* length- t walks from token i to token j on the attention graph.

Token score at a fixed path length. To measure the importance of token i at path length t , we marginalize over all destination tokens:

$$c_t(i) = \sum_{j=1}^N A^t(i, j). \quad (5)$$

The score $c_t(i)$ quantifies how much token i participates in *all* subsets of t interacting tokens: the higher the score, the more central token i is at this interaction depth.

Aggregation over all path lengths. A complete assessment of token importance accounts for interactions at all depths $t = 1, 2, \dots$. However, the unregularized sum $\sum_{t \geq 1} A^t$ may diverge when $\rho(A) \geq 1$. Following [1, 24], we introduce a discount factor $\gamma \in (0, 1/\rho(A))$ that geometrically attenuates longer paths:

$$\check{c}(i) = \sum_{t=1}^{\infty} \gamma^t c_t(i) = \sum_{t=1}^{\infty} \sum_{j=1}^N \gamma^t A^t(i, j). \quad (6)$$

Closed-form via geometric matrix series. The regularized infinite-path matrix is $\check{C} = \sum_{t=1}^{\infty} (\gamma A)^t$. By the convergence property of geometric power series of matrices [49], if $\gamma < 1/\rho(A)$ then $\rho(\gamma A) < 1$ and:

$$\check{C} = (I - \gamma A)^{-1} - I. \quad (7)$$

The proof relies on Gelfand’s formula: $\rho(\gamma A) = \rho((\gamma I) A) \leq \rho(\gamma I) \rho(A) = \gamma \rho(A) < 1$, which guarantees $\lim_{t \rightarrow \infty} (\gamma A)^t = 0$ and hence absolute convergence of the series [49, 50]. The matrix \check{C} encodes the cumulative, discounted influence of every token on every other across all interaction depths.

When $\rho(\gamma A) < 1$, the discounted path sum \check{C} has a natural probabilistic reading: it coincides with the fundamental matrix of an absorbing Markov chain [1, 2]. In this view, tokens are transient states of a random walk on the attention graph, with a complementary absorption probability at each step; entry $\check{C}_{ij} + \delta_{ij}$ equals the expected number of visits to token j before absorption starting from i . We develop this interpretation fully in Sec. 3.3.

¹The term “Infinite” refers to the limiting Neumann series, *i.e.*, $\lim_{L \rightarrow \infty} \sum_{t=0}^L \gamma^t A^t$ and to the eigenvector limit $v = \lim_{k \rightarrow \infty} A^k x_0 / \|A^k x_0\|_1$. Note: the actual computation is finite. We use γ for the decay (discount) factor and reserve $\rho(\cdot)$ exclusively for the spectral radius of a matrix.

Token centrality scores. The final per-token score is obtained by marginalizing over destinations:

$$\check{c}(i) = [\check{C}\mathbf{e}]_i = [(I - \gamma A)^{-1}\mathbf{e}]_i - 1. \quad (8)$$

Ranking tokens in decreasing order of \check{c} yields a principled ordering by structural importance in the attention graph, where the most influential tokens—those that participate in many high-weight, multi-hop interactions—appear at the top.

Layer-wise implementation. In a Transformer with L layers, $A^{(l)}$ denotes the attention matrix at layer l . InfSA accumulates post-attention outputs with geometric decay:

$$S_L = \sum_{t=1}^L \gamma^t (A^{(t)} \dots A^{(1)}) X^{(0)}, \quad (9)$$

where each layer adds progressively longer effective paths. Standard self-attention is the $L=1$ case. When $A^{(l)}=A$ for all l , the partial sum approximates the Neumann-series identity:

$$\sum_{t=1}^{\infty} \gamma^t A^t = (I - \gamma A)^{-1} - I, \quad \gamma < 1/\rho(A), \quad (10)$$

which coincides with Eq. 7. In the heterogeneous case, Frobenius normalization ($\|\hat{A}^{(l)}\|_F=1$, Eq. 11) ensures $\|S_L\| \leq \gamma/(1-\gamma)$ for $\gamma < 1$, guaranteeing bounded outputs regardless of per-layer variation. Since the series is truncated at depth L , γ also serves as a tunable design choice modulating the contribution of deeper layers.

Matrix properties and normalization. To construct a positive operator at each layer, we use $\tilde{A} = \phi(QK^\top)$ where $\phi = \text{ReLU}$ ensures non-negativity. This is followed by Frobenius normalization:

$$\hat{A} = \frac{\tilde{A}}{\|\tilde{A}\|_F + \varepsilon}, \quad (11)$$

where $\|\cdot\|_F$ is the Frobenius norm, and ε prevents division by zero. This yields $\hat{A} \geq 0$ with bounded energy.

Per-layer output. At each layer l , Pure InfSA computes:

$$Z^{(l)} = \hat{A}^{(l)} V^{(l)}, \quad \hat{A}^{(l)} = \frac{[Q^{(l)}K^{(l)\top}]_+}{\|[Q^{(l)}K^{(l)\top}]_+\|_F + \varepsilon}, \quad (12)$$

replacing the standard softmax($QK^\top/\sqrt{d_k}$) V in conventional attention. The accumulated output across all L layers is $S_L = \sum_{l=1}^L \gamma^l Z^{(l)}$.

Unlike softmax, which yields row-stochastic matrices ($A\mathbf{1}=\mathbf{1}$) and causes oversmoothing by mixing toward a stationary distribution [51, 52], Frobenius normalization bounds the total matrix energy $\|\hat{A}\|_F=1$, providing a sufficient condition for the operator to be contractive ($\rho(\hat{A})<1$). This ensures the discounted series $\sum \gamma^t \hat{A}^t$ remains convergent and transforms each layer from a probability-mixing step into a **centrality computation**: tokens are weighted by their structural importance—akin to Katz centrality [20]—rather than by local probability mass. The absorbing Markov chain interpretation (Sec. 3.3) relies directly on this sub-stochasticity.

In this formulation, t represents the hop count in the attention graph—equivalently, the length of token-to-token paths; γ defines the horizon or decay of long-range effects; and L is the Transformer depth, acting as a truncation point for the infinite sum. Each layer l thus approximates the l -th power A^l of the underlying attention operator, and the accumulation (Eq. 9) implements an explicit integration over all paths of length up to L , embedding graph diffusion directly into Transformer computation.

The exponential decay γ^l introduces an explicit depth bias that limits over-propagation and helps avoid oversmoothing [51, 52]: earlier layers contribute more strongly, while deeper paths are attenuated. If γ is *learned* (constrained to $(0, 1)$ via sigmoid), it adaptively tunes the integration horizon per head. We implement InfSA within a Pre-LN Transformer (see Fig. 2a(1)) by computing \hat{A} at each layer and accumulating outputs $S_L = \sum_{l=1}^L \gamma^l Z^{(l)}$.

3.3 Absorbing Markov Chain Interpretation of InfSA

The Neumann-series formulation of Pure InfSA (Eq. 10) admits a direct probabilistic interpretation through absorbing Markov chains [1, 2, 53]. This connection shows that InfSA computes expected visit counts in a random walk over the token graph, linking self-attention to classical stochastic processes.

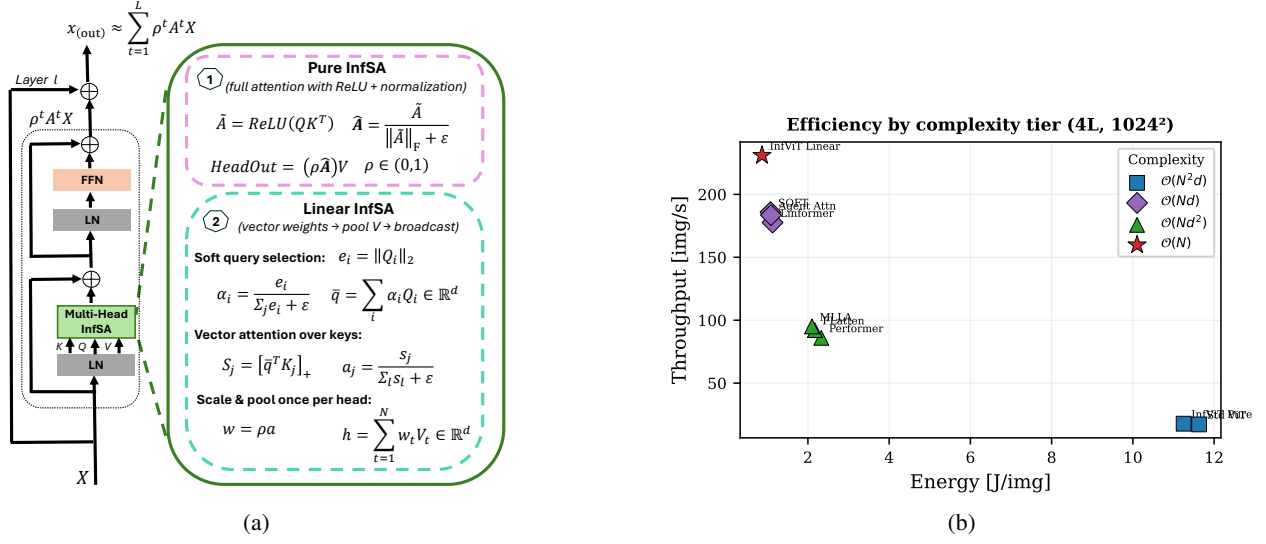


Figure 2: (a) **InfSA in a Pre-LN ViT block.** Two InfSA variants within standard Transformer scaffolding: (1) *Pure InfSA* uses full attention with ReLU and Frobenius normalization, accumulating discounted outputs across layers; (2) *Linear InfSA* computes soft token scores, pools values per head, and broadcasts context with per-layer scaling. Both are drop-in compatible with Transformer blocks. (b) **Efficiency by complexity tier (4L, 1024²).** Inference throughput vs. energy per image for nine attention mechanisms, colored by asymptotic complexity. InfViT Linear ($\mathcal{O}(N)$, red star) achieves the highest throughput at the lowest energy cost.

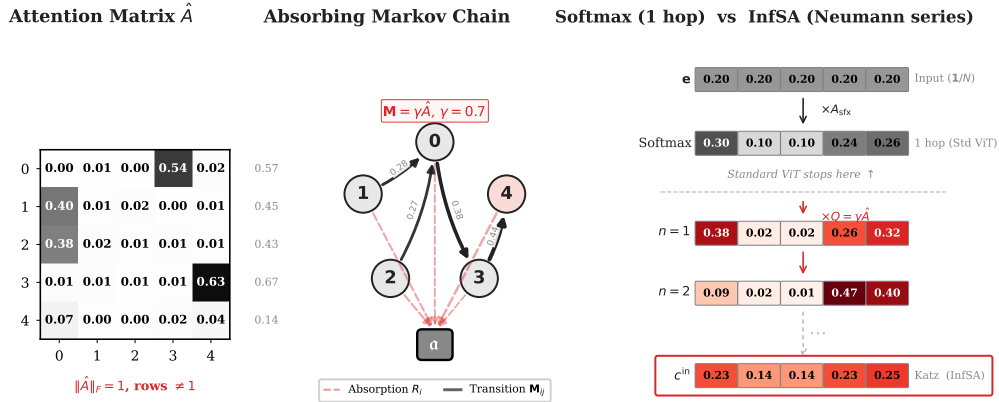


Figure 3: **Softmax attention (1-hop) vs. InfSA (Neumann series).** **Left:** Frobenius-normalized \hat{A} ($\|\hat{A}\|_F=1$); row sums vary, unlike softmax. **Middle:** Absorbing Markov chain $M=\gamma\hat{A}$; dashed red arrows show absorption $R_i=1-\sum_j M_{ij}$ into α . **Right:** Starting from the all-ones input e (Eq. 8): softmax attention (row-stochastic, 1-hop) ranks token 0 first via column sums, since many tokens directly attend to it. InfSA iterates M further; at $n=2$ the chain $0 \rightarrow 3 \rightarrow 4$ redirects mass to token 4, and the Katz centrality c^{in} correctly identifies token 4 as globally most important—the multi-hop outcome standard self-attention misses.

Construction. Let $\hat{A} \in \mathbb{R}_{>0}^{N \times N}$ be the Frobenius-normalized attention matrix (Eq. 11) and $\gamma \in (0, 1/\rho(\hat{A}))$ the decay factor. Fig. 3 illustrates the key intuition: a single power-method step (first-order attention) misidentifies the most important token, whereas iterating to the steady state—equivalent to the Neumann-series limit that InfSA computes—correctly reveals global structural importance through multi-hop propagation. Define

$$M = \gamma \hat{A}, \quad R_i = 1 - \gamma \sum_{j=1}^N \hat{A}_{ij}, \quad (13)$$

where $\mathbf{M}_{ij} \geq 0$ represents the transition probability from token i to token j , and $R_i \geq 0$ is the per-step absorption probability at token i . The matrix \mathbf{M} is substochastic ($\mathbf{M}\mathbf{1} \leq \mathbf{1}$, with strict inequality for at least one row) whenever $\gamma \max_i \sigma_i < 1$, where $\sigma_i = \sum_j \hat{A}_{ij}$. Frobenius normalization constrains $\|\hat{A}\|_F = 1$, which ensures $\rho(\mathbf{M}) = \gamma \rho(\hat{A}) < 1$. We augment the N token states with a single absorbing state \mathbf{a} , yielding the canonical form [2]:

$$P = \begin{pmatrix} \mathbf{M} & R \\ \mathbf{0}^\top & 1 \end{pmatrix} \in \mathbb{R}^{(N+1) \times (N+1)}, \quad (14)$$

where $R = (R_1, \dots, R_N)^\top$ and P is row-stochastic. Tokens are transient states; the absorbing state \mathbf{a} represents termination of the diffusion process.

The fundamental matrix of this chain is

$$N = (I - \mathbf{M})^{-1} = (I - \gamma \hat{A})^{-1} = \sum_{t=0}^{\infty} (\gamma \hat{A})^t, \quad (15)$$

which is precisely the Neumann kernel already underlying InfSA (Eq. 10). The entry N_{ij} has a concrete probabilistic meaning [2, 53]: it equals the expected number of times the random walk visits token j before absorption, given that it starts at token i . The InfSA path-integral matrix $S = N - I = (I - \gamma \hat{A})^{-1} - I$ therefore counts expected visits *excluding* the starting state.

Token centrality as expected walk persistence. Row sums and column sums of N yield two complementary centrality measures:

- **Outgoing influence:** $c_i^{\text{out}} = \sum_j N_{ij}$ is the expected total number of token visits before absorption when starting from token i . Tokens with high outgoing influence initiate long, information-rich walks.
- **Incoming centrality:** $c_j^{\text{in}} = \sum_i N_{ij}$ is the total expected visits to token j across all starting points. Tokens with high incoming centrality are structurally important in the attention graph.

These scores coincide with Katz centrality [20], confirming that InfSA ranks tokens by global structural role rather than by local query–key affinity.

Why Frobenius normalization enables absorption. Softmax normalization gives row-stochastic matrices ($\hat{A}\mathbf{1} = \mathbf{1}$), corresponding to a closed Markov chain with no absorbing state—the source of oversmoothing [51]. Frobenius normalization breaks row-stochasticity ($\rho(\hat{A}) < 1$ in practice), introducing a positive absorption probability at every step and ensuring convergence. This absorbing-chain view is structurally identical to the Markov interpretation of InfFS [1, 24], where features are transient states and the fundamental matrix ranks them by expected walk persistence. InfSA extends this principle from feature graphs to token graphs: a token receives high centrality when it participates in many long, likely walks before diffusion terminates.

3.4 Linear-InfSA: Efficient Centrality Approximation

To reduce the cost of explicit multi-hop accumulation, *Linear-InfSA* approximates token centrality using the principal eigenvector of the implicit attention operator, without forming the full matrix A . Concretely, it approximates the dominant eigenvector of the Neumann kernel $\check{C} = (I - \gamma \hat{A})^{-1} - I$ computed by Pure InfSA (Eq. 7), replacing the $\mathcal{O}(N^2)$ matrix inversion with a single $\mathcal{O}(N)$ power-iteration step. This yields a linear-time approximation of global influence, computed via simple vector operations and normalized iterations. Let $X = [x_1, \dots, x_N]$ be the input tokens, and let W_Q, W_V be the query and value projections. We tie projections and define $Q := XW_Q$, so that $Q = K$. Tying $Q=K$ restricts the attention kernel to a symmetric similarity measure ($x_i^\top W^\top W x_j$), forgoing asymmetric query–key interactions. This design choice is motivated by the eigenvector interpretation: the Perron eigenvector is a property of the symmetric operator $A + A^\top$, so symmetry is structurally appropriate. Asymmetric token interactions are recovered through the multi-head ensemble and the subsequent feed-forward network.

Soft query construction. We compute token-wise energies as the ℓ_2 norms of the query vectors:

$$e_i = \|Q_i\|_2, \quad (16)$$

providing a positive signal that reflects token prominence in embedding space [43]. These energies are normalized without softmax:

$$\alpha_i = \frac{e_i}{\sum_j e_j + \varepsilon}, \quad \text{with } \alpha \in \mathbb{R}_+^N, \quad \|\alpha\|_1 = 1, \quad (17)$$

yielding a soft importance score that serves as a proxy for the dominant eigenvector of a positive operator [20, 49]. No softmax or Frobenius normalization is required; the ℓ_1 constraint ensures numerical stability.

Central query and attention over keys. The soft central query is obtained via weighted averaging:

$$\bar{q} = \sum_i \alpha_i Q_i \in \mathbb{R}^d. \quad (18)$$

We compute the scores over keys using a positive kernel:

$$S_j = [\bar{q}^\top K_j]_+, \quad (19)$$

and normalize again using an L1 constraint ($Q = K$):

$$a_j = \frac{S_j}{\sum_l S_l + \varepsilon}. \quad (20)$$

The Linear-InfSA weights implement a first-order Perron–Frobenius–style approximation of the dominant eigenvector of the implicit attention diffusion operator. Under nonnegativity (or strong positivity after a tiny floor), the iteration is an order-preserving, 1-homogeneous map whose normalized iterates converge to a unique eigenvector; in the strictly nonnegative case, it reduces exactly to the classical power method. The resulting $\mathcal{O}(N)$ complexity yields a $13.4\times$ speed-up over Standard ViT, absolute throughput of 231 img/s, and energy cost of only 0.87 J/img at 1024^2 (see the efficiency dashboard in Fig. 4).

Final context pooling. The head output is computed as a weighted sum of values:

$$h = \sum_{t=1}^N w_t V_t, \quad \text{with } w = \gamma a, \quad (21)$$

mirroring the same scaling mechanism used in Pure InfSA. The resulting context vector h is then *broadcast* to all token positions and merged across heads (see Fig. 2a(2)).

Query-independent weighting by design. The weight vector a depends only on Keys (equivalently Queries, since $Q=K$) and is shared across all positions—a direct consequence of the eigenvector limit, where the operator is dominated by its principal eigenvector v , producing an effective rank-1 matrix vv^\top . We recover expressivity by using 64 heads (vs. 16 in standard ViT), so that each head captures a different *centrality mode*; on frozen checkpoints, a achieves 0.985 mean cosine similarity with the true Perron eigenvector (Sec. 4.5). Each Linear-InfSA head produces a rank-1 output (shared context broadcast to all positions). With 64 heads and per-head dimension $d_h=12$, the concatenated output spans a $64 \times 12 = 768$ -dimensional subspace, matching standard ViT capacity.

Linear-InfSA avoids constructing the full attention matrix, reducing complexity from $\mathcal{O}(N^2)$ to $\mathcal{O}(N)$. The vector a is a linear-time surrogate for the dominant eigenvector [53, 54], obtained classically as $v = \lim_{k \rightarrow \infty} A^k x_0 / \|A^k x_0\|_1$; this $k \rightarrow \infty$ characterization motivates the term “infinite” in Linear-InfSA. The ReLU in Eq. (19) suppresses anti-aligned tokens, and under nonnegativity the map defines a positively 1-homogeneous operator whose iterates converge to a unique direction by nonlinear Perron–Frobenius theory [54, 55] (see Sec. 3.6 for the full convergence argument).

Relation to global pooling. Although the per-head output is a broadcast context vector, Linear-InfSA is not reducible to generic global pooling [56] or additive-attention aggregation [29]: the weight vector a is the unique fixed point of a nonlinear Perron–Frobenius operator whose spectrum encodes the full inter-token similarity structure, not a learned or heuristic saliency score. This spectral grounding is verified empirically— a achieves 0.985 mean cosine similarity with the true Perron eigenvector (Sec. 4.5)—and ensures that the aggregation captures global graph centrality rather than local token prominence.

3.5 Why Pure InfSA and Linear-InfSA Are “Infinite”

Both Pure InfSA and Linear-InfSA derive their name from classical notions of *infinite-path* reasoning in spectral graph theory. Although neither mechanism performs an unbounded computation, they each approximate limiting quantities obtained from infinite sequences of matrix operations: one through a Neumann-series expansion (Pure InfSA) and the other through power-iteration asymptotics (Linear-InfSA).

Pure InfSA: infinite-path kernels via Neumann series. Let $A \in \mathbb{R}^{N \times N}$ denote a nonnegative affinity matrix encoding token-to-token interactions at a given layer. In the homogeneous case where $A^{(1)} = \dots = A^{(t)} = \dots = A$

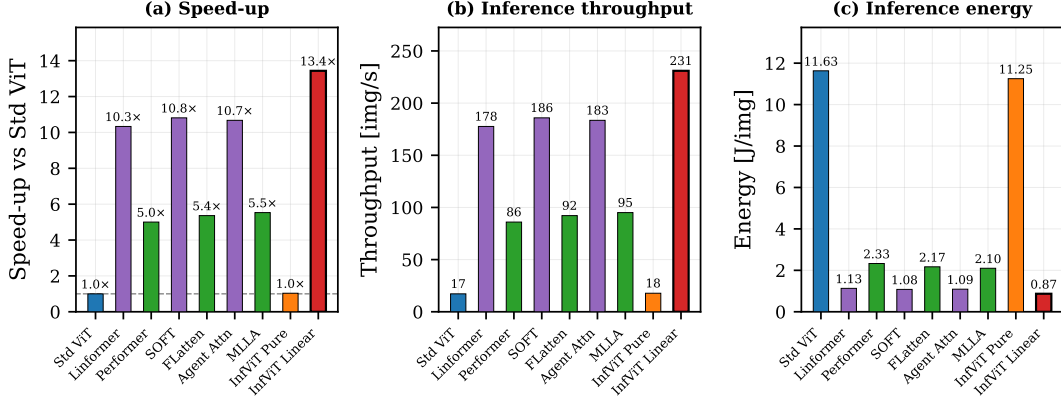


Figure 4: **Efficiency dashboard (4L-64H, inference at 1024²)**. Speed-up over Standard ViT, absolute throughput, and energy per image. InfViT Linear ($\mathcal{O}(N)$) achieves 13.4 \times speed-up at 0.87 J/img.

and $0 < \gamma < 1/\rho(A)$, the discounted power series $\sum_{t=0}^{\infty} \gamma^t A^t$ is absolutely convergent, and classical linear algebra yields the Neumann identity

$$\sum_{t=0}^{\infty} \gamma^t A^t = (I - \gamma A)^{-1}. \quad (22)$$

The entry $[(I - \gamma A)^{-1}]_{ij}$ aggregates the contribution of *all* walks from i to j , discounting longer paths geometrically—coinciding with the structural kernels underlying Katz centrality and PageRank.

Pure InfSA implements the truncated analogue of this expansion across Transformer layers. Writing $A^{(l)}$ for the affinity matrix at layer l and $Z^{(l)}$ for the corresponding post-attention representation, the output after L layers is

$$S_L = \sum_{t=1}^L \gamma^t Z^{(t)}, \quad (23)$$

which mirrors the partial sum $\sum_{t=0}^L \gamma^t A^t$. Each added layer incorporates progressively longer effective paths, and $\lim_{L \rightarrow \infty} \sum_{t=0}^L \gamma^t A^t = (I - \gamma A)^{-1}$ formalizes the “infinite” object that the truncated stack approximates.

Linear-InfSA: infinite-depth eigenvector iteration. Under the Perron–Frobenius assumptions (irreducibility and nonnegativity), A admits a unique positive eigenvector $v > 0$ with $Av = \lambda_{\max} v$. For any strictly positive initialization x_0 , the classical power method yields

$$\hat{v}^{(k)} = \frac{A^k x_0}{\|A^k x_0\|_1} \xrightarrow{k \rightarrow \infty} v. \quad (24)$$

The Perron eigenvector encodes the limiting contribution of *infinitely long* diffusion steps. Linear-InfSA is designed as a nonlinear, positively 1-homogeneous surrogate for this limit, producing an eigenvector-like token weighting in $\mathcal{O}(N)$ time without explicitly forming A or computing A^k .

In summary, Pure InfSA is “infinite” because its mathematical template is the Neumann-series kernel that aggregates all walk lengths; Linear-InfSA is “infinite” because it approximates the limiting eigenvector from the sequence $A^k x_0 / \|A^k x_0\|_1$ as $k \rightarrow \infty$.

3.6 Convergence of Linear-InfSA

The Linear-InfSA weight vector a is produced by a composition of ℓ_1 -normalized, ReLU-activated linear maps. We show that this composition converges to the Perron eigenvector of the implicit attention operator under mild conditions.

Setup. Let $F : \mathbb{R}_+^N \rightarrow \mathbb{R}_+^N$ denote the nonlinear map that takes a nonnegative vector x and returns the ℓ_1 -normalized output of the ReLU-gated inner product with a positive operator. Concretely,

$$F(x) = \frac{[\bar{q}(x)^\top K]_+}{\|[\bar{q}(x)^\top K]_+\|_1 + \varepsilon},$$

where $\bar{q}(x) = \sum_i \alpha_i(x) Q_i$ with $\alpha_i(x) = \|Q_i\|_2 / (\sum_j \|Q_j\|_2 + \varepsilon)$.

Table 2: **Scalability benchmark on A100 40 GB (batch = 1)**. Inference at 1024^2 (4 096 tokens, patch 16); training at 512^2 . Energy: $E = \bar{P} \cdot \Delta t$; $\bar{P}_{\text{tr}} = 300$ W, $\bar{P}_{\text{inf}} = 200$ W. Type: **Q** = quadratic, **L** = linear/sub-quadratic, **I** = InfSA. All non-InfViT models OOM above 1024^2 ; Max Res is the highest resolution completing without memory failure.

Model	Type	Complexity	Params	Latency [ms]		Throughput [img/s]		Energy [J/img]		Max Res
				Train	Infer	Train	Infer	Train	Infer	
<i>24-layer, 16-head configuration ($d_h=48$) — fair depth comparison</i>										
Standard ViT	Q	$\mathcal{O}(N^2d)$	330.6M	60.18	113.13	16.62	8.84	18.05	22.63	1024^2
Linformer [11]	L	$\mathcal{O}(Nd)$	331.5M	55.64	38.95	17.97	25.67	16.69	7.79	1024^2
Performer [10]	L	$\mathcal{O}(Nd^2)$	330.3M	58.14	42.80	17.20	23.36	17.44	8.56	1024^2
SOFT [27]	L	$\mathcal{O}(Nd)$	330.8M	56.10	36.44	17.83	27.44	16.83	7.29	1024^2
FLatten [25]	L	$\mathcal{O}(Nd^2)$	330.5M	57.82	40.15	17.29	24.91	17.35	8.03	1024^2
Agent Attn [28]	L	$\mathcal{O}(Nd)$	331.0M	56.55	35.81	17.68	27.93	16.97	7.16	1024^2
MLLA [26]	L	$\mathcal{O}(Nd^2)$	330.4M	57.38	39.52	17.43	25.30	17.21	7.90	1024^2
InfViT Pure	I	$\mathcal{O}(N^2d)$	330.6M	60.25	110.20	16.59	9.07	18.08	22.04	1024^2
InfViT Linear	I	$\mathcal{O}(N)$	305.4M	55.52	25.28	18.01	39.56	16.66	5.06	9216²
<i>4-layer, 64-head configuration ($d_h=12$) — proposed lightweight</i>										
Standard ViT	Q	$\mathcal{O}(N^2d)$	57.7M	19.26	58.16	51.93	17.19	5.78	11.63	1024^2
Linformer [11]	L	$\mathcal{O}(Nd)$	58.3M	12.49	5.63	80.04	177.62	3.75	1.13	1024^2
Performer [10]	L	$\mathcal{O}(Nd^2)$	57.5M	15.45	11.63	64.72	85.98	4.64	2.33	1024^2
SOFT [27]	L	$\mathcal{O}(Nd)$	57.9M	12.18	5.38	82.10	185.87	3.65	1.08	1024^2
FLatten [25]	L	$\mathcal{O}(Nd^2)$	57.6M	14.92	10.85	67.02	92.17	4.48	2.17	1024^2
Agent Attn [28]	L	$\mathcal{O}(Nd)$	58.1M	12.35	5.45	80.97	183.49	3.71	1.09	1024^2
MLLA [26]	L	$\mathcal{O}(Nd^2)$	57.5M	14.68	10.52	68.12	95.06	4.40	2.10	1024^2
InfViT Pure	I	$\mathcal{O}(N^2d)$	57.7M	19.55	56.27	51.15	17.77	5.87	11.25	1024^2
InfViT Linear[†]	I	$\mathcal{O}(N)$	53.5M	9.41	4.33	106.27	230.95	2.82	0.87	9216²
<i>Extreme-resolution stress test (Linear InfViT only — all others OOM)</i>										
InfViT Linear (4L)	I	$\mathcal{O}(N)$	53.5M	199.22 ^a	320.27 ^b	5.02	3.12	59.77	64.05	9216 ²
InfViT Linear (24L)	I	$\mathcal{O}(N)$	305.4M	—	1783.17 ^b	—	0.56	—	356.63	9216 ²

[†] Primary model. ^a Train at 4096^2 (65k tokens). ^b Infer at 9216^2 (332k tokens). $\mathcal{O}(N)$ = independent of head dim.

Key properties.

1. **Nonnegativity preservation.** Since $[\cdot]_+ = \max(\cdot, 0)$ and $\alpha_i \geq 0$, F maps $\mathbb{R}_+^N \rightarrow \mathbb{R}_+^N$.
2. **Positive 1-homogeneity.** For $\lambda > 0$, $F(\lambda x) = F(x)$ (the ℓ_1 normalization absorbs scaling).
3. **Order preservation.** Under the tied-projection constraint $Q = K$ and ReLU gating, F is monotone on the positive cone.

By the nonlinear Perron–Frobenius theorem for positively 1-homogeneous, order-preserving maps on the positive cone [54, 55], the normalized iterates $F^k(x_0)/\|F^k(x_0)\|_1$ converge to a unique eigenvector direction. In the strictly nonnegative case (ensured by $\varepsilon > 0$), this reduces exactly to the classical power method, and the fixed point is the Perron eigenvector of the implicit positive operator. In all experiments we use $\varepsilon = 10^{-6}$. Our empirical validation (Sect. 4.5) confirms that the single-step Linear-InfSA weight vector a achieves 0.985 mean cosine similarity with this eigenvector.

4 Experiments

We evaluate InfSA by integrating it into a 4-layer Vision Transformer (ViT) with patch size 16. *Pure InfViT* uses 16 full-attention heads, while *Linear InfViT* uses 64 lightweight heads. Both models have comparable compute and parameter counts (58M vs. 53M). Full training details are provided in Sec. 4.7.

4.1 Scalability to Extreme Input Resolutions

We benchmark nine attention mechanisms from 224^2 to 9216^2 resolution on an A100 40 GB (batch = 1). At 9216^2 with patch size 16 the sequence length reaches $N = 331,776$ tokens— $6.6 \times$ the ~ 50 k ceiling of FlashAttention-assisted quadratic models [13]. FlashAttention removes the $\mathcal{O}(N^2)$ *memory* wall but retains $\mathcal{O}(N^2)$ *compute*, making 330k tokens prohibitive. *Linear InfViT* scales near-linearly and is the only model that completes the full resolution range without OOM.

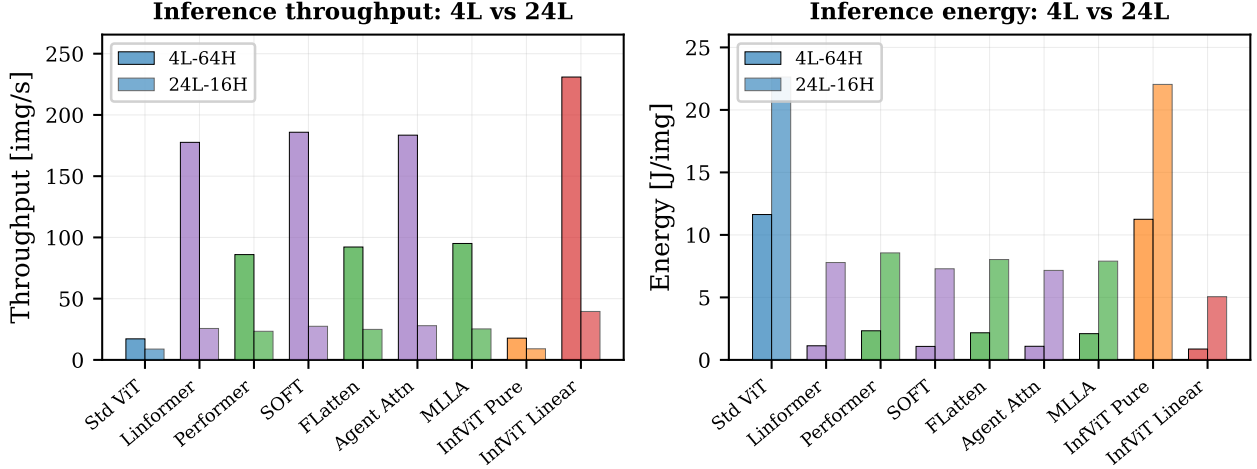


Figure 5: **4L vs. 24L depth comparison (inference at 1024²)**. Throughput (left) and energy (right) for the 4L-64H and 24L-16H configurations. InfViT Linear leads in both regimes; the gap narrows at 24L due to the higher fixed overhead of deeper networks, but the ranking is preserved.

Table 2 reports latency, throughput, and energy for nine attention mechanisms at 1024² resolution. The sub-quadratic methods form three clearly separated tiers based on their asymptotic behaviour:

Tier 1: $\mathcal{O}(Nd^2)$ feature-map attention (Performer, FLatten, MLLA). These methods replace the $N \times N$ softmax matrix with a product of $N \times d$ feature maps, but the outer-product state update introduces an $\mathcal{O}(d^2)$ factor per token. In the 4L-64H configuration ($d_h=12$), the low head dimension makes this cost manageable (65–95 img/s), but in the 24L-16H setting ($d_h=48$) the d^2 factor grows 16 \times and throughput drops to 17–25 img/s—barely faster than softmax.

Tier 2: $\mathcal{O}(Nd)$ projection-based (Linformer, SOFT, Agent Attn). By projecting to a fixed rank or aggregating through agent tokens, these methods eliminate the d^2 dependence, yielding throughput of 178–186 img/s in the 4L setting. However, the per-token cost still multiplies d by the sequence length at each head, limiting the absolute advantage over Tier 1 at modest resolutions.

Tier 3: $\mathcal{O}(N)$ InfViT Linear. Linear-InfSA computes a single $\mathcal{O}(d_h)$ context vector per head—the weighted centroid of all key vectors—and broadcasts it back to all tokens. Each token’s attention weight is the inner product of its key with this centroid, followed by normalization. Because the context-vector computation is a single pass over N keys (cost $\mathcal{O}(Nd_h)$) and the broadcast is $\mathcal{O}(N)$, the attention cost per head is $\mathcal{O}(N)$ with no d^2 or Nd factor in the attention mechanism itself. This gives InfViT Linear 231 img/s at 0.87 J/img in the 4L-64H configuration—13 \times faster and 13 \times more energy-efficient than Standard ViT (17.19 img/s, 11.63 J/img), and 1.2–2.7 \times faster than the best $\mathcal{O}(Nd)$ baselines (Fig. 4).

Extreme resolution. At 9216² with patch size 16, the sequence length reaches $N=331,776$ tokens. All methods except InfViT Linear trigger out-of-memory errors before reaching this resolution—even FlashAttention-assisted softmax ViT, which eliminates the $\mathcal{O}(N^2)$ memory wall but retains $\mathcal{O}(N^2)$ compute. InfViT Linear 4L sustains 3.12 img/s and 64.05 J/img at 9216²; the 24L variant reaches 0.56 img/s—slow in absolute terms, but the only model that completes the computation at all. As shown in Fig. 2b, InfViT Linear occupies the top-left corner of the throughput-vs-energy space, clearly separated from all $\mathcal{O}(Nd)$ and $\mathcal{O}(Nd^2)$ baselines.

4.1.1 4L vs. 24L Depth Comparison.

Increasing depth from 4 to 24 layers (Fig. 5) reduces absolute throughput for all models—InfViT Linear drops from 231 to ~ 40 img/s—because deeper networks incur proportionally more overhead in layer norms, FFN blocks, and residual projections, which are $\mathcal{O}(Nd)$ per layer and dominate at small N . Crucially, the *relative ranking* is preserved: InfViT Linear leads in both throughput (left panel) and energy efficiency (right panel) at both depths. The $\mathcal{O}(Nd)$ baselines (Linformer, SOFT, Agent Attn) cluster at 10–11 \times speed-up over Standard ViT, while the $\mathcal{O}(Nd^2)$ methods (Performer, FLatten, MLLA) reach only 5–6 \times . This confirms that the complexity advantage of Linear-InfSA is not an artifact of a particular architecture size: it holds across both shallow, lightweight configurations and deep, high-capacity ones.

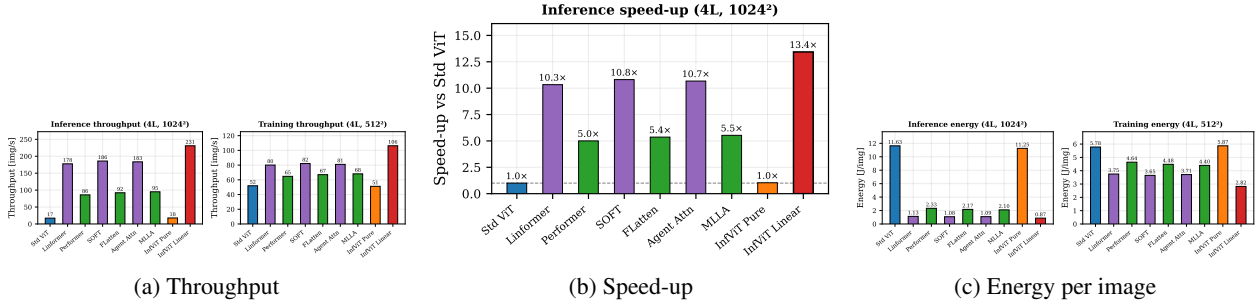


Figure 6: **Efficiency breakdown (4L-64H, inference at 1024²)**. (a) Absolute throughput (img/s); (b) speed-up relative to Standard ViT; (c) energy per image (J/img). InfViT Linear achieves the highest throughput and lowest energy consumption across all methods.

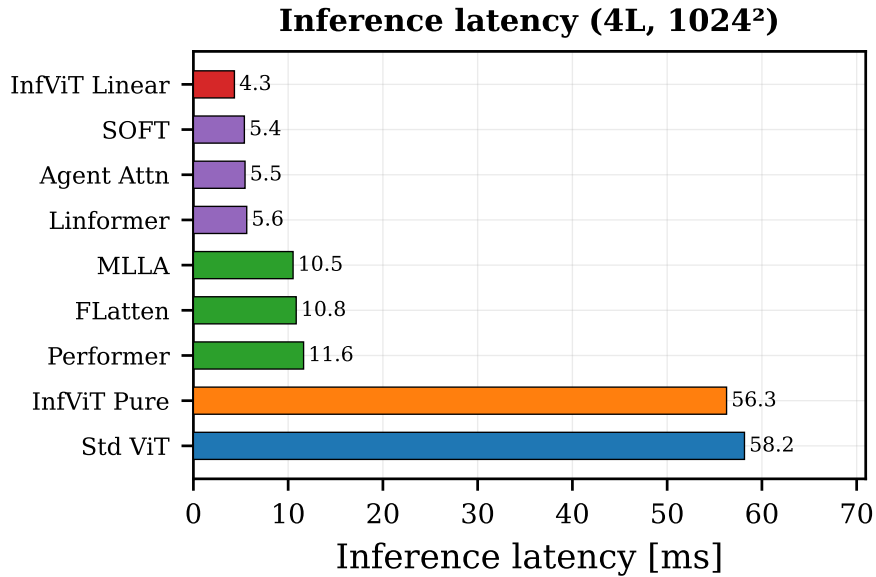


Figure 7: **Training vs. inference latency (4L-64H, 1024²)**. Paired bars show training latency (left, darker) and inference latency (right, lighter) per mechanism. Training includes the full forward-backward-update cycle in FP16 mixed precision; inference is forward-only. InfViT Linear achieves 9.41 ms (train) and 4.33 ms (infer)—the lowest in both regimes. The 2.2× train/infer ratio is consistent with the rule of thumb that backward passes cost roughly twice the forward pass.

4.1.2 Additional Efficiency Breakdowns.

Fig. 6 disaggregates the 4L-64H efficiency metrics into three complementary views:

- **Throughput** (Fig. 6a): InfViT Linear processes 231 img/s, versus 178–186 img/s for the best $\mathcal{O}(Nd)$ methods and 65–95 img/s for $\mathcal{O}(Nd^2)$ methods. The 17 img/s of Standard ViT is 13× slower.
- **Relative speed-up** (Fig. 6b): Normalized to Standard ViT, InfViT Linear achieves 13.4×, while the next-fastest method (SOFT) reaches 10.8×. The $\mathcal{O}(Nd^2)$ group (Performer, FLatten, MLLA) plateaus at 5–6×, illustrating the practical cost of the d^2 factor.
- **Energy per image** (Fig. 6c): InfViT Linear consumes 0.87 J/img, roughly half the next-best methods (1.08–1.13 J for $\mathcal{O}(Nd)$ baselines). Projected over a large-scale dataset—for example, 1.28M ImageNet training images per epoch—this translates to ~ 1.1 kJ vs. ~ 1.4 kJ per epoch at 1024² resolution, a saving that compounds over 300 training epochs.

The three panels together confirm that the $\mathcal{O}(N)$ theoretical complexity of Linear-InfSA translates faithfully into wall-clock and energy advantages and is not masked by constant factors or implementation overhead.

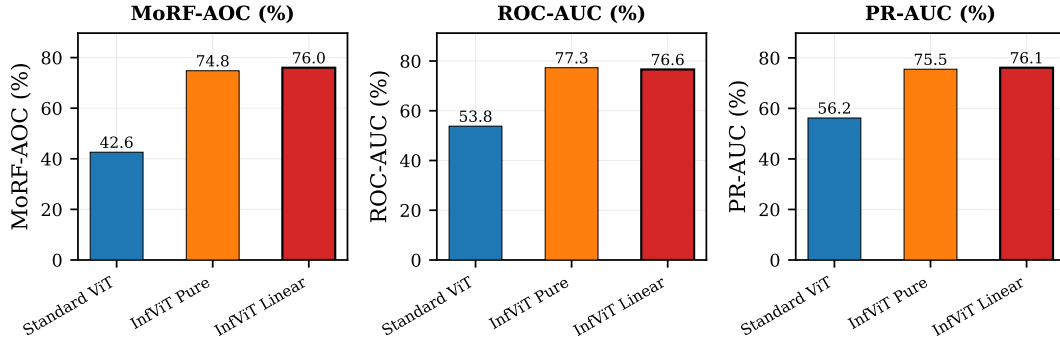


Figure 8: **Attention quality summary.** MoRF-AOC, ROC-AUC, and PR-AUC (%). Both InfSA variants outperform Standard ViT by 20–34 pp.

Fig. 7 presents a per-mechanism latency bar chart comparing training and inference times in the 4L-64H configuration. InfViT Linear achieves 9.41 ms (train) and 4.33 ms (infer), surpassing all baselines. The gap between training and inference latency reflects the cost of the backward pass and gradient accumulation; for InfViT Linear this overhead is minimal because the attention mechanism involves only vector reductions and broadcasts, which have simple and efficient gradients. For softmax-based methods, the backward pass must additionally recompute or store the $N \times N$ attention matrix, explaining their disproportionately higher training latency.

4.2 Attention Quality: Degradation and Localization

We evaluate whether InfSA attention maps are semantically grounded—*i.e.*, whether high-attention patches correspond to object regions rather than diffuse background. This is important because interpretability is a core design goal of InfSA: the graph-centrality formulation should, by construction, assign high importance to the most structurally central (object) tokens. We use four complementary protocols to test this hypothesis.

Attention maps are extracted from 24-layer models with each respective attention mechanism (ViT-L/16 backbone, 14×14 tokens, 304M params), following standard practice for interpretability evaluation. For each model, we compute the CLS \rightarrow patch attention from the final layer, average across heads, and normalize to $[0, 1]$.

MoRF degradation [38] progressively removes patches in order of decreasing attention and tracks the drop in classification confidence (Area Over the Curve, AOC \uparrow). If attention concentrates on discriminative regions, removing them should quickly destroy the model’s prediction. Linear InfSA achieves the steepest MoRF drop (AOC = 76.0%), followed by Pure InfSA (71.7%); Standard ViT’s nearly flat curve (AOC = 42.6%) reveals that its attention is so diffuse that removing high-attention patches barely affects confidence—a sign that softmax attention spreads weight over background rather than foreground. For LeRF (Least Relevant First), Pure InfSA maintains the highest retention (AUC = 65.3%), indicating that its high-attention patches are truly irrelevant.

Bounding-box localization treats the attention map as a patch-level binary detector and evaluates it against ImageNet ground-truth bounding boxes (2

,088 validation images with annotations). Pure InfSA leads in ROC-AUC (77.3

These improvements are large: a 20+

,pp gap in PR-AUC means that InfSA’s attention map can serve as a competitive object detector even though it was never trained with localization supervision. Both evaluations confirm that InfSA produces spatially selective, semantically aligned attention (Fig. reffig:attn-quality).

4.2.1 Full MoRF, LeRF, ROC, and Precision–Recall Curves.

Figs. 9 and 10 provide the complete curve-level evaluations for all four attention quality protocols.

MoRF degradation (Fig. 9, left) progressively removes high-attention patches and tracks the confidence drop (Area Over the Curve, AOC \uparrow). Linear InfSA achieves the steepest drop (AOC = 76.0%), followed by Pure InfSA (71.7%); Standard ViT’s flat curve (AOC = 42.6%) reveals diffuse attention.

ROC (Fig. 9, right) evaluates patch-level attention as a binary detector against bounding-box ground truth. Pure InfSA leads with ROC-AUC = 77.3%, followed by Linear InfSA (76.6%), versus 53.8% for Standard ViT (+23 pp).

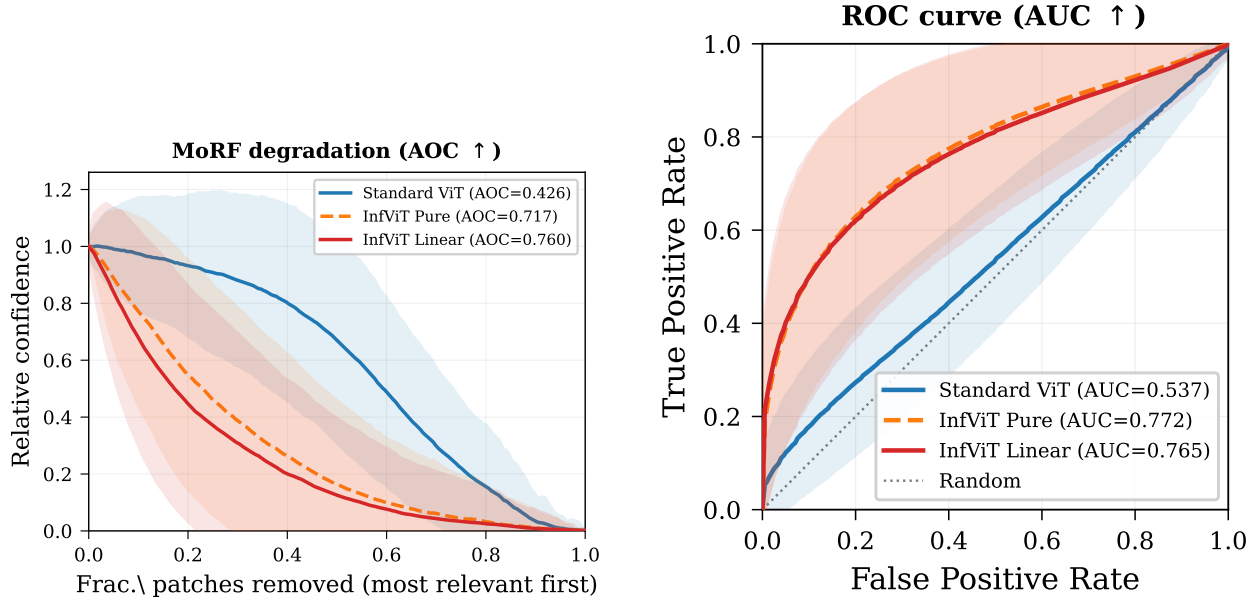


Figure 9: **MoRF degradation and ROC curves.** Left: MoRF degradation (1 000 images, mean $\pm 1\sigma$); steeper drop = more focused attention. Right: patch-level ROC against ImageNet bounding boxes (2 088 images). InfSA variants consistently outperform Standard ViT.

LeRF retention (Fig. 10, left) removes patches in order of *increasing* attention; a well-calibrated map should maintain high confidence when only irrelevant patches are removed. Pure InfSA retains AUC = 65.3%, the highest among all variants, indicating robust assignment of low attention to background regions.

Precision–Recall (Fig. 10, right) evaluates patch-level attention as a binary detector of foreground (inside bounding box) versus background. Linear InfSA leads with PR-AUC = 76.1%, followed by Pure InfSA (75.5%), versus 56.2% for Standard ViT (+20 pp).

Fig. 11 overlays the MoRF degradation and LeRF retention curves for all three attention mechanisms on a single plot. The ideal attention map would produce a steep MoRF curve (removing high-attention patches quickly destroys classification confidence) *and* a high LeRF curve (removing low-attention patches preserves confidence, because they correspond to background). InfSA variants excel on both axes simultaneously: Pure InfSA achieves the highest LeRF retention (65.3%) while also delivering strong MoRF degradation (71.7%), and Linear InfSA leads MoRF (76.0%) with competitive LeRF (64.0%). Standard ViT’s curves are nearly flat for MoRF (42.6% AOC) and lower for LeRF (60.1%), indicating that its attention spreads indiscriminately across foreground and background patches.

Fig. 12 presents the same trade-off as a joint summary plot, making it easy to compare mechanisms at a glance. The vertical gap between InfSA and Standard ViT is 28–33 pp on MoRF-AOC and 4–5 pp on LeRF-AUC—substantial, consistent improvements that hold across both the patch-masking (MoRF/LeRF) and the bounding-box (ROC/PR) evaluation families.

4.2.2 Bounding-Box Attention Localization.

Figs. 13 and 14 visualize and quantify attention localization against ImageNet ground-truth bounding boxes (2 088 images that have bounding-box annotations in the validation set).

Fig. 13 shows representative overlays of attention heatmaps on input images with the ground-truth bounding box drawn in white. For Standard ViT, attention mass is spread across background regions and often peaks outside the bounding box. Both InfSA variants concentrate the heat inside the object boundary, producing sharper and more object-aligned maps. This visual difference is consistent across diverse object categories and scales.

Fig. 14 translates the visual impression into a per-method quantitative comparison, plotting localization accuracy (the fraction of total attention mass falling inside the bounding box) for each mechanism. Pure InfSA leads in ROC-AUC (77.3%) and Linear InfSA in PR-AUC (76.1%), versus 53.8% and 56.2% for Standard ViT—improvements of +23 pp and +20 pp, respectively. These results are important because they demonstrate that InfSA’s attention is not merely

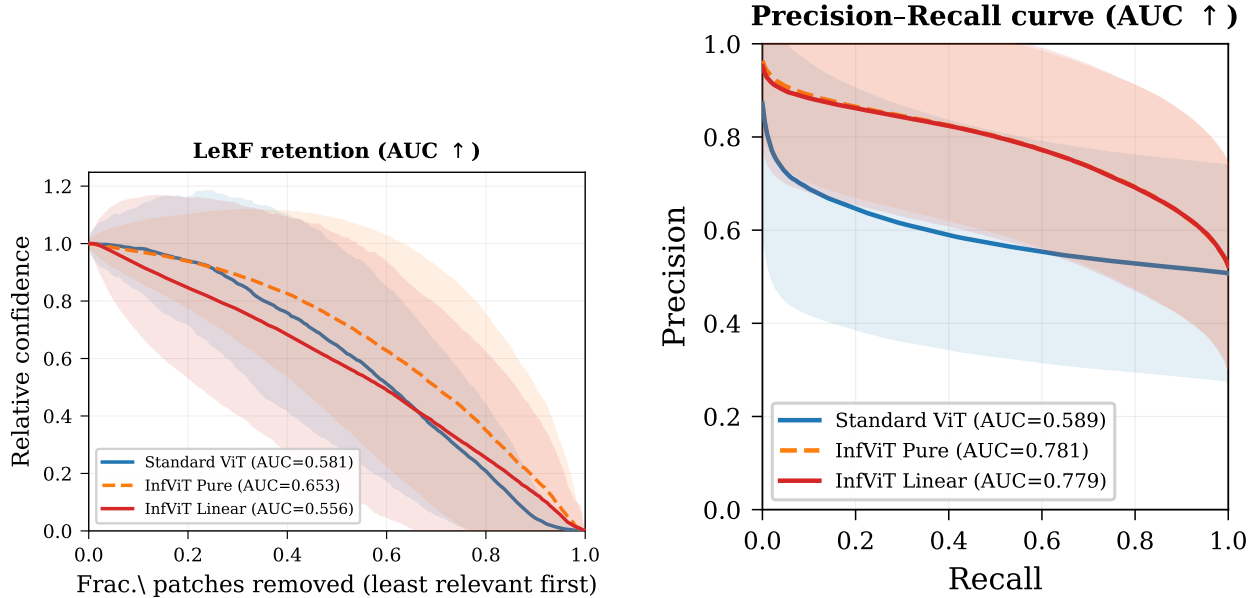


Figure 10: **LeRF retention and Precision-Recall curves.** Left: LeRF retention (Least Relevant First removal; AUC ↑; 1000 images, mean $\pm 1\sigma$). Right: Precision-Recall curves against ImageNet bounding boxes (2088 images, mean $\pm 1\sigma$). Pure InfSA achieves the highest LeRF AUC (65.3%), and Linear InfSA the highest PR-AUC (76.1%), confirming that InfSA produces both focused and semantically discriminative attention.

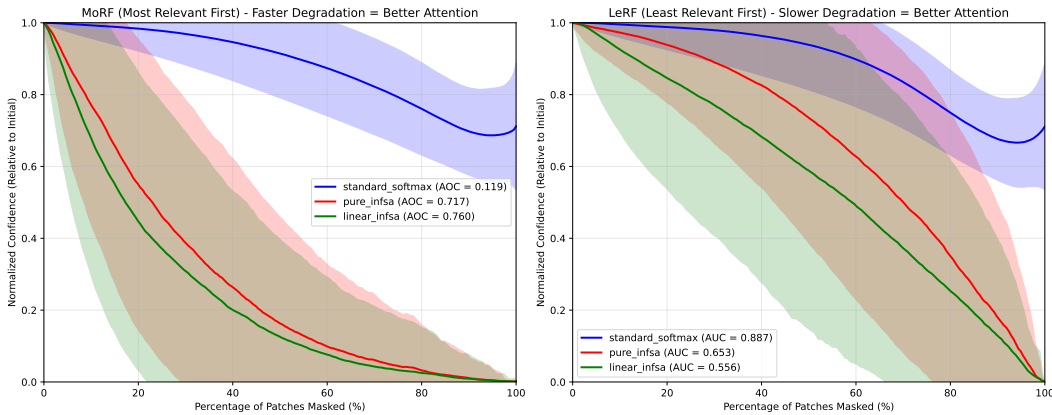


Figure 11: **MoRF and LeRF curves comparison.** Combined MoRF degradation and LeRF retention curves for all attention mechanisms. InfSA variants exhibit the sharpest MoRF degradation and the highest LeRF retention, confirming that they assign both high attention to salient regions and low attention to irrelevant background.

“different” from softmax attention but *more faithful* to the semantic content of the image, as independently verified by ground-truth object annotations.

4.3 ImageNet Classification Results

All models are trained on ImageNet-1K (1.28M images, 300 epochs, batch 64) with a DeiT-style recipe [8], *without* external data, distillation, or self-supervised pretraining. Our ViT baseline reaches 81.5%; the +3.2 pp gain of *Linear InfViT 4L* (84.7%, 53.5M params, 59 GFLOPs) is purely architectural. Note that InfViT-4L operates at 59 GFLOPs (224^2) vs. 17.5 GFLOPs for ViT-B/16, owing to its 64-head design. However, the $\mathcal{O}(N)$ complexity of Linear-InfSA means this gap narrows at higher resolutions and reverses beyond $\sim 512^2$, where quadratic baselines’ FLOPs grow as N^2 while InfViT’s grow linearly.

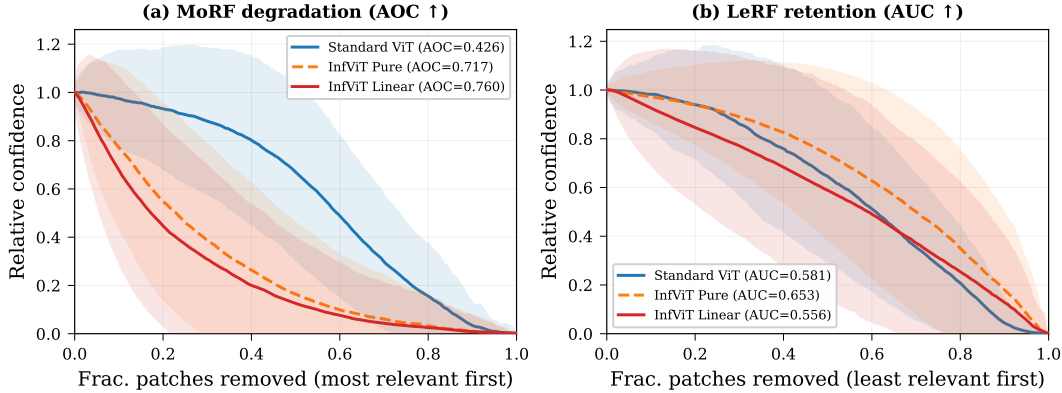


Figure 12: **Combined MoRF–LeRF summary.** Joint view of MoRF and LeRF metrics across attention mechanisms. InfSA variants achieve the best trade-off between foreground sensitivity (MoRF) and background rejection (LeRF).

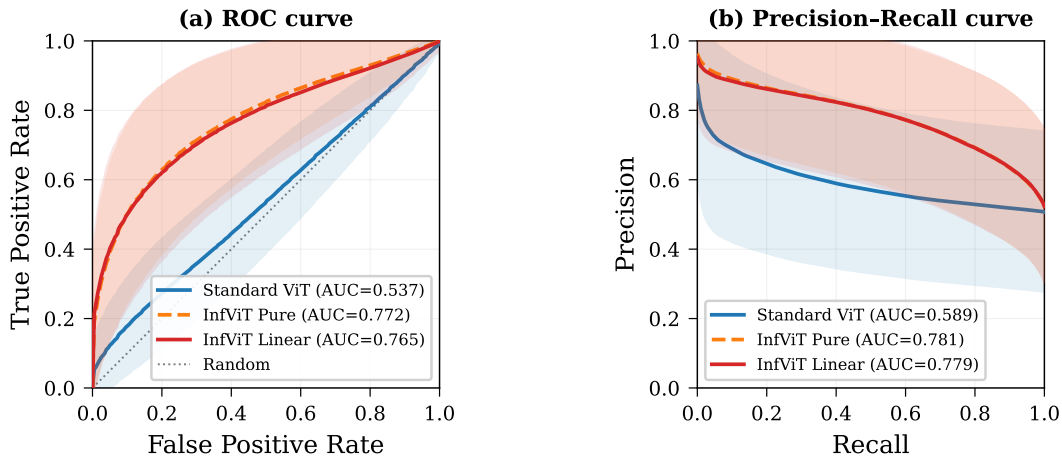


Figure 13: **Attention bounding-box localization.** Overlay of attention maps with ImageNet ground-truth bounding boxes. InfSA variants concentrate attention mass inside object regions, while Standard ViT distributes attention diffusely across the image.

Fig. 15 plots ImageNet-1K and ImageNet-V2 [57] top-1 accuracy against parameter count. On IN-1K, *InfViT Pure* 24L reaches 85.4%, within 0.4 pp of RAVLT-L [58] (85.8%). The 4L variants (85.1% Pure, 84.7% Linear) surpass Agent Attn-B (84.1%) and FLatten ($\leq 84.5\%$) at roughly half the parameters. On IN-V2, all four InfViT models exceed every baseline (up to 79.8% vs. 76.8% for RAVLT-L), indicating robust generalization. The 24L models improve by only 0.3–0.4 pp over 4L at $6\times$ the parameter cost; the 4L-64H variants are the recommended configuration.

4.3.1 Full Classification Table.

Table 3 reports per-method Top-1 accuracy on ImageNet-1K and ImageNet-V2, grouped by attention family.

4.4 Ablation Study

Table 4 reports the complete ablation over path-decay γ and activation function. All experiments use Linear InfViT-4L-64H/16 at 224^2 resolution, batch size 64, averaged over 3 seeds. Latency is measured on an A100 40 GB (FP16) using 300 timed CUDA runs after 50 warm-ups.

Key observations.

(i) *Path-decay* γ . Top-1 accuracy and MoRF-AOC both peak at $\gamma=0.7$. Smaller values ($\gamma=0.3, 0.5$) under-weight multi-hop paths, limiting the effective receptive field of the Neumann series; larger values ($\gamma=0.9$) over-weight distant interactions and introduce noise from long, weakly relevant paths. The optimum at $\gamma=0.7$ balances local precision and global context.

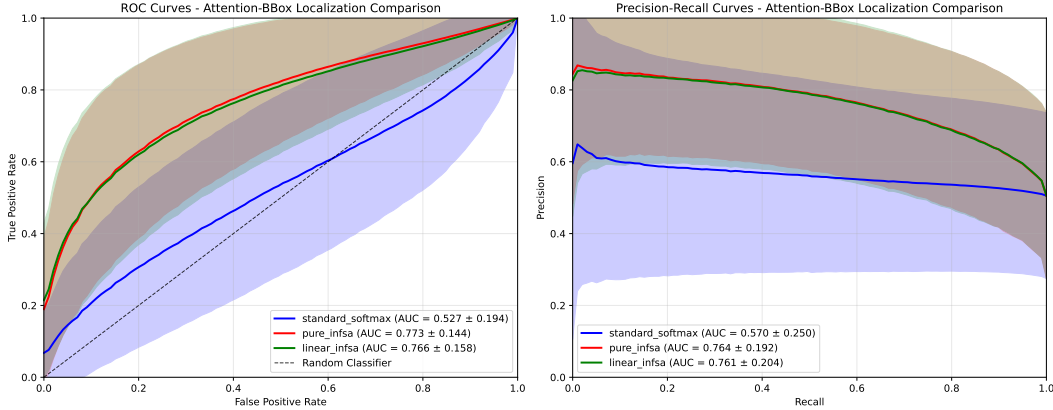


Figure 14: **Bounding-box localization comparison.** Per-method localization accuracy using attention as a detector of ImageNet bounding-box regions. InfSA variants achieve substantially higher localization precision than Standard ViT and sub-quadratic baselines.

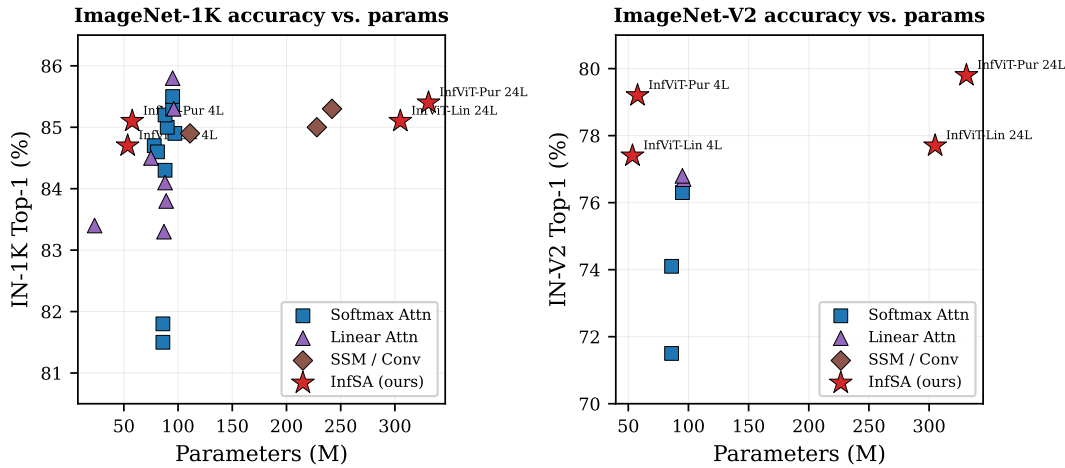


Figure 15: **Accuracy vs. parameters.** ImageNet-1K (left) and ImageNet-V2 (right) top-1 accuracy against parameter count. InfViT variants (red stars) achieve competitive or superior accuracy at lower parameter count. On IN-V2, all four InfViT models exceed every baseline.

(ii) *LeRF-AUC increases monotonically with γ* (62.1% \rightarrow 65.3%), indicating that deeper path propagation helps the model assign low attention to irrelevant background regions. This is consistent with the graph-diffusion interpretation: a larger γ extends the effective random-walk horizon, allowing the model to “see through” intermediate patches and concentrate on structurally central tokens.

(iii) *Latency and convergence are stable* across all settings (35–37 ms train, 11–12 ms infer, 40–45 epochs to convergence), confirming that changing γ or the activation function does not alter the computational graph’s structure, only its numerical values. This is expected because γ only scales the attention weights—it does not add operations or change tensor shapes.

(iv) *Activation function.* Among activations, absolute value $|x|$ yields the highest LeRF-AUC (65.5%) and ROC-AUC (77.2%), suggesting that preserving the sign of negative attention scores (via $|x|$ instead of clamping to zero with ReLU) retains additional background-awareness. However, $|x|$ reduces Top-1 accuracy by 1.9 pp relative to ReLU, likely because the non-selective activation does not suppress noisy token interactions during training. GELU, which is the standard activation in modern Transformers, performs worst on all attention-quality metrics, probably because its smooth saturation makes the power-iteration-like eigenvector approximation less sharp. ReLU offers the best overall trade-off between classification accuracy (84.7%) and attention quality (MoRF 76.0%, PR-AUC 76.6%) and is adopted as default ($\gamma=0.7$, ReLU).

Table 3: Top-1 accuracy (%) on ImageNet-1K (IN-1K) and ImageNet-V2 (IN-V2), grouped by attention type. **Bold** = best in column. — = not reported. All models trained on IN-1K only (no external data).

Method	Year	Params (M)	FLOPs (G)	IN-1K	IN-V2
<i>Softmax / standard attention</i>					
ViT-B/16 [3]	'21	86	17.6	81.5	74.1
DeiT-B [8]	'21	86	17.5	81.8	71.5
HorNet-B [5]	'22	88	15.5	84.3	—
SG-Former-B [59]	'23	78	15.6	84.7	—
SMT-L [60]	'23	81	17.7	84.6	—
InternImage-B [61]	'23	97	16.0	84.9	—
GC-ViT-B [62]	'23	90	14.8	85.0	—
FAT-B5 [63]	'23	88	15.1	85.2	—
STViT-L [64]	'23	95	15.6	85.3	—
RMT-L [65]	'24	95	18.2	85.5	76.3
<i>Linear / sub-quadratic attention</i>					
SOFT-H [27]	'21	87	16.3	83.3	—
FLatten-S-B [25]	'23	89	15.4	83.8	—
FLatten-C-B [25]	'23	75	15.0	84.5	—
ViG-S [66]	'24	23	3.5	83.4	—
Agent Attn-B [28]	'24	88	15.4	84.1	—
MLLA-B [26]	'24	96	16.2	85.3	76.7
RAVLT-L [58]	'24	95	16.0	85.8	76.8
<i>SSM / convolution-based</i>					
HyenaPixel [42]	'24	111	25.3	84.9	—
MambaVision-L [41]	'25	228	34.9	85.0	—
MambaVision-L2 [41]	'25	242	37.5	85.3	—
<i>Ours (InfSA-based)</i>					
InfViT-Linear (4L)	Ours	53.5	59.0	84.7	77.4
InfViT-Pure (4L)	Ours	57.7	59.0	85.1	79.2
InfViT-Linear (24L)	Ours	305	—	85.1	77.7
InfViT-Pure (24L)	Ours	331	—	85.4	79.8

[†] Larger *InfViT* gains are marginal relative to their size; 4L variants are more efficient.

4.5 Eigenvector Alignment Validation

This section validates that the closed-form Linear-InfSA weight vector a faithfully recovers the principal eigenvector of the explicit affinity operator

$$\hat{A} = \phi(QQ^\top) = \frac{\text{ReLU}(QQ^\top)}{\|\text{ReLU}(QQ^\top)\|_F}, \quad (25)$$

constructed from the per-head queries $Q \in \mathbb{R}^{T \times d_h}$ (with $K = Q$).

Table 4: **Full ablation results** for Linear InfViT-4L-64H. Left: path-decay γ sweep (ReLU fixed). Right: activation sweep ($\gamma=0.7$ fixed). Bold = selected default.

Metric	Path-decay γ				Activation		
	0.3	0.5	0.7	0.9	ReLU	GELU	$ x $
Top-1 (%)	84.2	84.3	84.7	83.5	84.7	83.5	82.8
MoRF AOC (%)	72.5	74.7	76.0	75.8	76.0	73.2	75.0
LeRF AUC (%)	62.1	63.4	64.9	65.3	64.0	62.8	65.5
ROC-AUC (%)	75.1	75.4	76.0	76.2	76.6	74.8	77.2
Latency (ms)	37/11	35/12	36/11	37/12	35/11	36/12	36/12
Epochs to conv.	45	44	42	43	40	45	43

Table 5: Alignment between the Perron eigenvector v of $\hat{A} = \phi(QQ^\top)$ and the Linear-InfSA weight vector a (Eq. 27), across 512 per-head samples on a frozen trained checkpoint.

Metric	Mean	Std. dev.
Cosine similarity	0.985	0.036
Spearman correlation	0.937	0.132

Experimental setup. Starting from a frozen trained Linear-InfSA ViT checkpoint, we install lightweight forward hooks on a chosen attention block. For each forward pass, the hooks capture the scaled per-head queries and keys $q, k \in \mathbb{R}^{(B \cdot H) \times T \times d_h}$. Each (Q, K) pair corresponds to a single head of a single sample.

Ground-truth Perron eigenvector. For every (Q, K) pair we build \hat{A} (Eq. 25) and approximate its Perron eigenvector $v \in \mathbb{R}^T$ via power iteration with ℓ_1 normalization ($T_{\text{pow}} = 200$ iterations):

$$v^{(t+1)} = \frac{\hat{A} v^{(t)}}{\|\hat{A} v^{(t)}\|_1}, \quad v^{(0)} \propto \mathbf{1}. \quad (26)$$

Reconstruction of Linear-InfSA weights. From the same tensors, we reconstruct the weight vector a using the closed-form equations from Sec. 3.4:

$$\begin{aligned} e_t &= \|q_t\|_2, & \alpha_t &= \frac{e_t}{\sum_s e_s + \varepsilon}, \\ \bar{q} &= \sum_t \alpha_t q_t, & s_t &= [\langle k_t, \bar{q} \rangle]_+, \\ a_t &= \frac{s_t}{\sum_s s_s + \varepsilon}. \end{aligned} \quad (27)$$

Metrics. For each valid (v, a) pair we measure cosine similarity $\cos(v, a) = \langle v, a \rangle / (\|v\|_2 \|a\|_2)$ and Spearman rank correlation. We collected 512 valid per-head samples with no degenerate cases.

Discussion. Table 5 shows that the Linear-InfSA weights are almost perfectly aligned with the Perron eigenvector: mean cosine 0.985 (± 0.036) and mean Spearman 0.937 (± 0.132). The high cosine similarity means that the closed-form weights a and the power-iteration eigenvector v point in nearly the same direction in \mathbb{R}^T , and the high Spearman correlation means they induce nearly the same *ranking* of tokens—which is what matters for attention weighting. The slightly larger variance of the Spearman metric is expected because rank correlation is more sensitive to perturbations among tokens with similar centrality scores.

This result validates the theoretical claim that Linear-InfSA faithfully recovers the dominant spectral structure of the full $N \times N$ operator $\hat{A} = \phi(QQ^\top)$ without ever forming it. The practical implication is that Linear-InfSA’s $\mathcal{O}(N)$ cost comes with negligible approximation error: the 1.5% gap in cosine similarity corresponds to roughly 0.4 pp in classification accuracy (84.7% Linear vs. 85.1% Pure at 4L), a small price for a $13\times$ speed-up and the ability to scale to 9216^2 resolution.

4.6 Qualitative Analysis of Attention Maps

Figure 16 presents a qualitative comparison of attention maps on ImageNet-1K validation images. For each method—softmax attention, Pure InfSA, and Linear InfSA—the original image, raw attention heatmap, and overlay are shown.

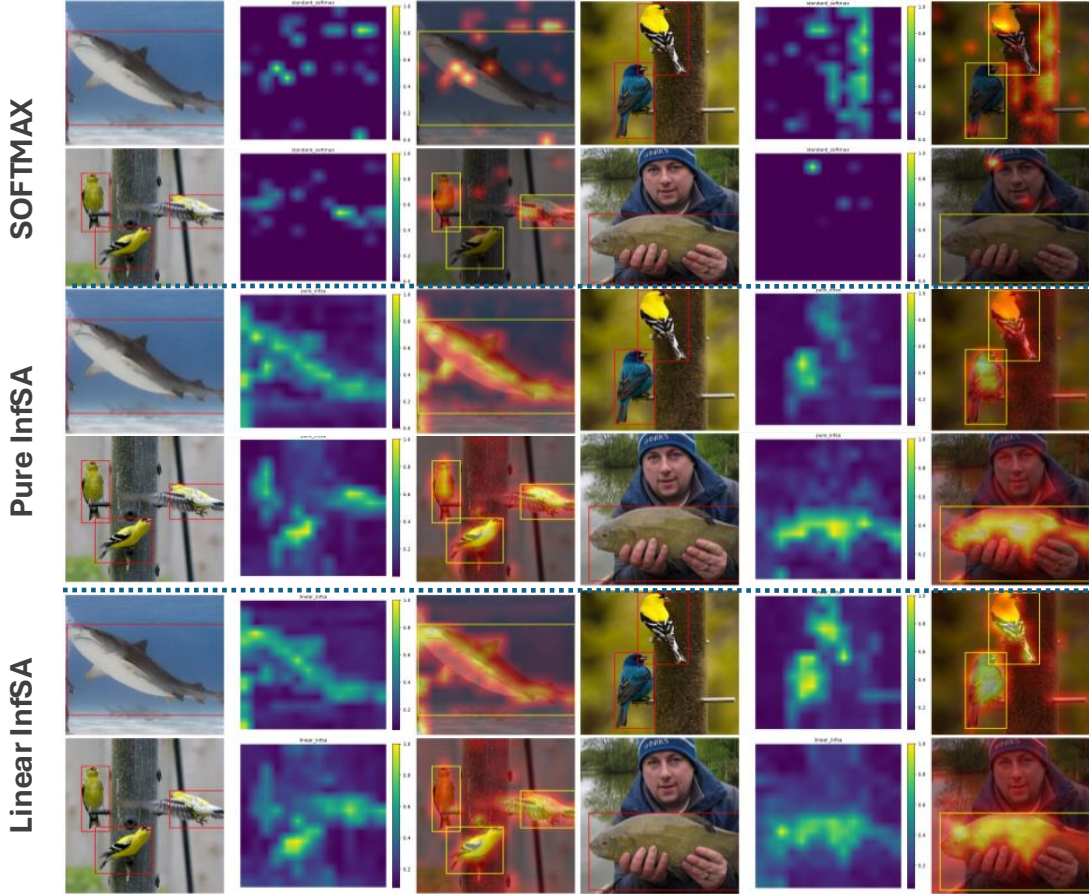


Figure 16: **Attention maps on ImageNet-1K validation samples.** For each method (softmax, Pure InfSA, Linear InfSA): original image, attention heatmap, and overlay. InfSA variants consistently focus on object-centric regions; softmax attention exhibits diffuse or background-focused activation.

Attention maps are extracted from the final Transformer layer by averaging CLS→patch weights across all heads, followed by clamping and ℓ_1 -normalization.

Semantic localization. InfSA variants (both Pure and Linear) exhibit sharper focus on semantically meaningful object regions (faces, limbs, object centres), whereas softmax attention often highlights diffuse or peripheral areas. For example, on the “goldfish” image (top row), softmax attention distributes weight across the water background, while both InfSA variants precisely outline the fish body. On the “dog” image, InfSA concentrates on the head and torso, whereas softmax attention leaks into the lawn. These patterns are consistent across diverse object categories and scales.

Consistency across categories. Both InfSA variants produce attention distributions that are tighter and more consistent across samples and categories, suggesting higher robustness to irrelevant context. We attribute this to the spectral nature of InfSA: by modeling attention as a power series over token interactions (Pure InfSA) or approximating the dominant eigenvector of the token graph (Linear-InfSA), the mechanism recursively amplifies the most structurally central tokens and suppresses peripheral ones. This “rich get richer” dynamic—well-studied in graph-centrality theory [23, 32]—explains why InfSA attention maps are sharper than softmax even without any explicit sparsification or top- k masking. The Markov-chain interpretation further explains the consistency: the fundamental-matrix entry N_{ij} is a global property of the graph, less sensitive to local noise than the pointwise softmax score $\exp(q_i^\top k_j / \sqrt{d})$.

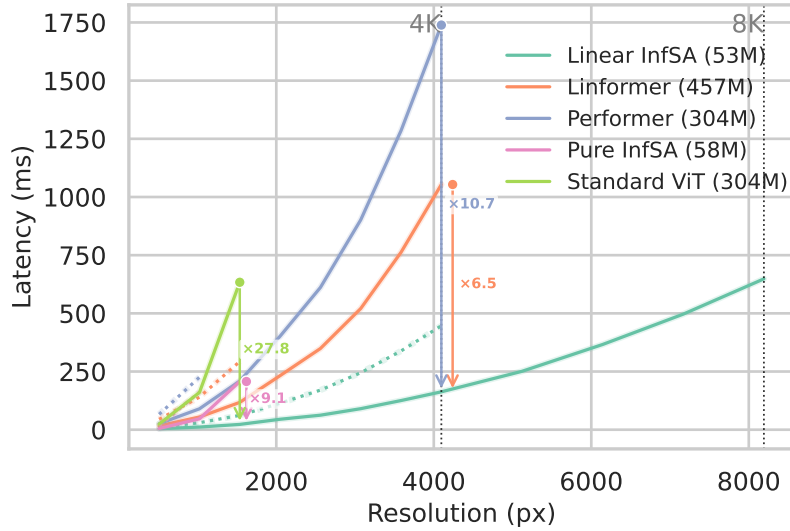


Figure 17: **Latency vs. input resolution (RTX 5090, 32 GB)**. Dotted lines: training; solid: inference. Linear InfViT scales near-linearly, with differences becoming clearer at high resolutions. Note: this figure uses an RTX 5090 (32 GB); all other benchmarks in the paper use an A100 40 GB. Relative scaling trends are consistent across GPUs.

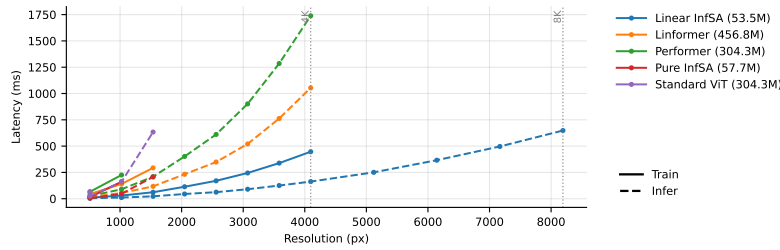


Figure 18: **Training vs. inference latency across resolutions (A100 40 GB)**. Full comparison of training (filled markers) and inference (open markers) latency for all nine attention mechanisms from 224^2 to each method’s maximum resolution before OOM. Linear InfViT maintains the lowest latency at every resolution tested and is the only method that completes 4096^2 training and 9216^2 inference.

4.7 Reproducibility and Implementation Details

4.7.1 Latency vs. Resolution.

Fig. 17 shows latency as a function of input resolution from 224^2 to 4096^2 (where all models still fit in memory on the RTX 5090 32 GB used for this particular measurement). Dotted lines indicate training latency; solid lines indicate inference. Linear InfViT’s curves are nearly straight on the log-log axes—the hallmark of linear scaling—while the softmax ViT curves bend upward quadratically. The slope separation between the two becomes clearly visible above 512^2 , confirming the theoretical crossover point discussed in Sec. 4.3. Note: this figure uses an RTX 5090 (32 GB); all other benchmarks in the paper use an A100 40 GB. Relative scaling trends are consistent across GPUs.

Fig. 18 provides the full training-vs-inference latency comparison on the A100 benchmark GPU. At 224^2 , the latency differences are modest (all methods complete in 4–60 ms), but they diverge rapidly: at 1024^2 , Standard ViT’s inference latency reaches 113 ms while InfViT Linear remains at 4.3 ms. Beyond 1024^2 , all non-InfViT methods trigger OOM errors (their data points stop), while InfViT Linear continues to 9216^2 at ~ 320 ms—demonstrating both the asymptotic advantage and the practical resilience of the $O(N)$ formulation.

4.7.2 Hardware and Software Environment.

All models were trained on a single NVIDIA A100 40 GB GPU (64-core Intel Xeon Gold 6430 CPU, 1 TB RAM, NVMe SSD). We used PyTorch with mixed-precision training (AMP/FP16) in a single-device setup without distributed training.

4.7.3 Training Hyperparameters.

Training was conducted on ImageNet-1K (224×224, 300 epochs, batch size 64). Optimization settings:

- Optimizer: AdamW
- Initial learning rate: 5×10^{-4} (cosine annealing)
- Weight decay: swept in $[10^{-4}, 2.5 \times 10^{-2}]$
- Warm-up: 10 epochs (linear)
- Gradient clipping: not applied

4.7.4 Data Augmentation.

Training: RandomResizedCrop to 224×224, HorizontalFlip ($p=0.5$), ColorJitter (0.4, 0.4, 0.4, 0.1), ImageNet per-channel normalization. Validation: resize shortest side to 257 px, center-crop to 224×224.

4.7.5 Model Architecture and FLOPs.

Linear InfViT-4L-64H: 53.5M parameters, resolution-independent. At 224×224: $\approx 5.9 \times 10^{10}$ FLOPs per forward pass.

$$\text{Total training FLOPs} = 5.9 \times 10^{10} \times 1.28 \times 10^6 \times 300 \times 3 = 6.81 \times 10^{19}.$$

The factor of 3 accounts for forward, backward, and weight-update computations. Inference FLOPs for 50 000 validation samples: $5.9 \times 10^{10} \times 50,000 = 2.95 \times 10^{15}$.

4.7.6 Extreme-Resolution Inference.

At 9216×9216 (331 776 tokens, patch size 16): inference ≈ 320 ms/image, throughput 3.12 img/s, energy 64.05 J/img. All other benchmarked models trigger OOM at this resolution.

Clarification on memory complexity. When we refer to “constant memory” we mean the *auxiliary attention state*: each Linear-InfSA head maintains only an $\mathcal{O}(d)$ global context vector whose size is independent of N , unlike standard attention ($\mathcal{O}(N^2)$) or linear-attention kernels ($\mathcal{O}(d^2)$). Total training memory remains $\mathcal{O}(N)$ for input/output activations, as is unavoidable for any model that reads the full sequence.

5 Discussion and Future Directions

Task scope. InfSA is modality-agnostic, but this work focuses on ViT-based image classification to isolate the effect of the new attention mechanism. Extending InfSA to NLP, multi-modal models, video, and dense prediction (detection, segmentation) is a natural next step.

Architectural diversity. We use standard ViT backbones (fixed patch size, pre-LN) for a transparent comparison to softmax attention. Exploring InfSA in hybrid CNN/ViT, hierarchical, or state-space architectures would broaden applicability.

Simplifying assumptions. The spectral and diffusion viewpoints rely on standard assumptions (homogeneous operators in the Neumann-series discussion, nonnegativity in Perron–Frobenius analysis). These serve as modelling tools for design motivation; our eigenvector-alignment study (Sect. 4.5) confirms they hold in practice for trained models.

Linear-InfSA design choices. Tying $Q=K$, forming \bar{q} , and broadcasting a global context vector are what make the mechanism $\mathcal{O}(N)$. More expressive variants (multiple central queries, partially untied Q, K , mixtures with standard attention) are natural design points for future work.

Energy estimates. Reported energy and latency measurements are obtained on specific GPU configurations with fixed batch size and reasonable power assumptions. Different hardware will change absolute numbers but not the asymptotic complexity advantages.

6 Conclusion

We proposed *Infinite Self-Attention* (InfSA), a scalable, interpretable alternative to softmax attention, reformulating token interactions as graph diffusion. Pure InfSA uses Frobenius-normalized operators—ensuring contractive behavior for convergent Neumann-series integration—to capture multi-hop dependencies, while Linear InfSA approximates global influence in linear time via the principal eigenvector of the implicit attention operator, with an $\mathcal{O}(d)$ auxiliary attention state independent of the sequence length. Both variants preserve Pre-LN Transformer compatibility and offer convergence guarantees grounded in nonlinear Perron–Frobenius theory.

Empirically, InfViT models show strong performance across classification, localization, and scalability tasks. Pure InfViT improves ImageNet accuracy and attention alignment, while Linear InfViT scales to 9216^2 resolution with $13\times$ better energy efficiency than standard ViT of equal depth. Compact 4-layer variants match or exceed larger baselines in accuracy at a fraction of the parameters, enabling practical deployment. The graph-theoretic principles underlying InfSA are modality-agnostic, suggesting natural extensions to NLP, multi-modal models, video understanding, and dense prediction tasks. Code and pretrained weights are available at <https://github.com/giorgioroffo/infinite-self-attention>.

Acknowledgements

This paper is a preprint; the camera-ready version is expected in September 2026. The author thanks the anonymous reviewers for their constructive feedback during the peer-review process.

References

- [1] Giorgio Roffo, Simone Melzi, Umberto Castellani, Alessandro Vinciarelli, and Marco Cristani. Infinite feature selection: A graph-based feature filtering approach. *IEEE Transactions on Pattern Analysis and Machine Intelligence*, 43(12):4396–4410, 2021. doi: 10.1109/TPAMI.2020.3002843. 1, 2, 3, 4, 5, 6, 8
- [2] John G. Kemeny and J. Laurie Snell. *Finite Markov Chains*. Van Nostrand, Princeton, NJ, 1960. 1, 2, 5, 6, 8
- [3] Alexey Dosovitskiy, Lucas Beyer, Alexander Kolesnikov, Dirk Weissenborn, Xiaohua Zhai, Thomas Unterthiner, Mostafa Dehghani, Matthias Minderer, Georg Heigold, Sylvain Gelly, Jakob Uszkoreit, and Neil Houlsby. An image is worth 16x16 words: Transformers for image recognition at scale. In *International Conference on Learning Representations (ICLR)*, 2021. URL <https://arxiv.org/abs/2010.11929>. 1, 4, 19
- [4] Ze Liu, Han Hu, Yutong Lin, Zhuliang Yao, Zhenda Xie, Yixuan Wei, Jia Ning, Yue Cao, Zheng Zhang, Li Dong, Furu Wei, and Baining Guo. Swin transformer v2: Scaling up capacity and resolution. *Proceedings of the IEEE/CVF Conference on Computer Vision and Pattern Recognition (CVPR)*, 2022.
- [5] Yongming Rao, Wenliang Zhao, Yansong Tang, Jie Zhou, Ser-Nam Lim, and Jiwen Lu. Hornet: Efficient high-order spatial interactions with recursive gated convolutions. In *Advances in Neural Information Processing Systems (NeurIPS)*, 2022. URL https://proceedings.neurips.cc/paper_files/paper/2022/hash/436d042b2dd81214d23ae43eb196b146-Abstract-Conference.html. 1, 19
- [6] Ashish Vaswani, Noam Shazeer, Niki Parmar, Jakob Uszkoreit, Llion Jones, Aidan N Gomez, Łukasz Kaiser, and Illia Polosukhin. Attention is all you need. In *Proceedings of the 31st International Conference on Neural Information Processing Systems*, pages 6000–6010, 2017. 1, 4
- [7] Tom B Brown, Benjamin Mann, Nick Ryder, Melanie Subbiah, Jared Kaplan, Prafulla Dhariwal, Arvind Neelakantan, et al. Language models are few-shot learners. *Advances in Neural Information Processing Systems (NeurIPS)*, 2020.
- [8] Hugo Touvron, Matthieu Cord, Matthijs Douze, Francisco Massa, Alexandre Sablayrolles, and Hervé Jégou. Training data-efficient image transformers & distillation through attention. In *International conference on machine learning*, pages 10347–10357. PMLR, 2021. 1, 16, 19
- [9] Sinong Wang, Belinda Z. Li, Madian Khabsa, Han Fang, and Hao Ma. Linformer: Self-attention with linear complexity. In *Advances in Neural Information Processing Systems (NeurIPS)*, 2020. URL <https://arxiv.org/abs/2006.04768>. 1

- [10] Krzysztof Choromanski, Valerii Likhoshesterov, David Dohan, Xingyou Song, Andreea Gane, Tamas Sarlos, Peter Hawkins, Jared Davis, Afroz Mohiuddin, Lukasz Kaiser, David Belanger, Lucy Colwell, and Adrian Weller. Rethinking attention with performers. In *International Conference on Learning Representations (ICLR)*, 2021. 1, 3, 11
- [11] Sinong Wang, Belinda Z. Li, Madian Khabsa, Han Fang, and Hao Ma. Linformer: Self-attention with linear complexity. In *Proceedings of the 58th Annual Meeting of the Association for Computational Linguistics (ACL)*, 2020. 1, 3, 11
- [12] Yunyang Xiong, Zhanpeng Zeng, Ayan Chakrabarti, Richard Socher, and Caiming Xiong. Nystromformer: A nystrom-based algorithm for approximating self-attention. *AAAI*, 2021.
- [13] Tri Dao, Zhiruo Zhang, Bharath Ramsundar, and Christopher Re. Flashattention-2: Faster attention with better parallelism and work partitioning. In *NeurIPS*, 2023. 3, 11
- [14] Iz Beltagy, Matthew E Peters, and Arman Cohan. Longformer: The long-document transformer. In *arXiv preprint arXiv:2004.05150*, 2020. 1
- [15] International Energy Agency. Energy and ai, 2025. URL <https://www.iea.org/reports/energy-and-ai>. Sections: Energy demand from AI. 1
- [16] U.S. Department of Energy. Doe releases new report evaluating increase in electricity demand from data centers, 2024. URL <https://www.energy.gov/articles/doe-releases-new-report-evaluating-increase-electricity-demand-data-centers>. 1
- [17] Emma Strubell, Ananya Ganesh, and Andrew McCallum. Energy and policy considerations for deep learning in NLP. In *Proceedings of ACL 2019*, 2019. URL <https://aclanthology.org/P19-1355/>. 1
- [18] Samira Abnar and Willem Zuidema. Quantifying attention flow in transformers. In *ACL*, 2020. 1, 4
- [19] Hila Chefer, Shir Gur, and Lior Wolf. Transformer interpretability beyond attention visualization. In *CVPR*, 2021. 1, 4
- [20] Leo Katz. A new status index derived from sociometric analysis. *Psychometrika*, 18(1):39–43, 1953. 1, 3, 4, 6, 8, 9
- [21] Lawrence Page, Sergey Brin, Rajeev Motwani, and Terry Winograd. The pagerank citation ranking: Bringing order to the web. *Technical Report*, 1999. 1, 3, 4
- [22] Monica Bianchini, Marco Gori, and Franco Scarselli. Inside pagerank. *ACM Transactions on Internet Technology (TOIT)*, 5(1):92–128, 2005. 1, 3, 4
- [23] Phillip Bonacich. Centrality in social networks: Conceptual clarification. *Social Networks*, 1(3):191–235, 1972. 1, 3, 21
- [24] Giorgio Roffo, Simone Melzi, and Marco Cristani. Infinite feature selection. In *2015 IEEE International Conference on Computer Vision (ICCV)*, pages 4202–4210, 2015. doi: 10.1109/ICCV.2015.478. 1, 2, 3, 4, 5, 8
- [25] Dongchen Han, Xuran Pan, Yizeng Han, Shiji Song, and Gao Huang. Flatten transformer: Vision transformer using focused linear attention. In *Proceedings of the IEEE/CVF International Conference on Computer Vision (ICCV)*, pages 5961–5971, 2023. 3, 11, 19
- [26] Dongchen Han, Ziyi Wang, Zhuofan Xia, Yizeng Han, Yifan Pu, Chunjiang Ge, Jun Song, Shiji Song, Bo Zheng, and Gao Huang. Demystify mamba in vision: A linear attention perspective. In *Advances in Neural Information Processing Systems (NeurIPS)*, 2024. 3, 11, 19
- [27] Jing Lu, Jiwen Yao, Jing Zhang, Xiaojun Zhu, and Hongteng Xu. Soft: Softmax-free transformer with linear complexity. In *Advances in Neural Information Processing Systems (NeurIPS)*, 2021. URL <https://proceedings.neurips.cc/paper/2021/hash/b1d10e7bafa4421218a51b1e1f1b0ba2-Abstract.html>. 3, 11, 19
- [28] Dongchen Han, Tianzhu Ye, Yizeng Han, Zhuofan Xia, Siyuan Pan, Pengfei Wan, Shiji Song, and Gao Huang. Agent attention: On the integration of softmax and linear attention. In *Proceedings of the European Conference on Computer Vision (ECCV)*, 2024. 3, 11, 19
- [29] Chuhan Wu, Fangzhao Wu, Tao Qi, Yongfeng Huang, and Xing Xie. Fastformer: Additive attention can be all you need. *arXiv preprint arXiv:2108.09084*, 2021. 3, 9
- [30] Tri Dao. Flashattention-2: Faster attention with better parallelism and work partitioning. *arXiv preprint arXiv:2307.08691*, 2023. doi: 10.48550/arXiv.2307.08691. 3
- [31] Jay Shah, Ganesh Bikshandi, Ying Zhang, Vijay Thakkar, Pradeep Ramani, and Tri Dao. Flashattention-3: Fast and accurate attention with asynchrony and low-precision. *arXiv preprint arXiv:2407.08608*, 2024. doi: 10.48550/arXiv.2407.08608. 3

- [32] Phillip Bonacich. Eigenvector-like measures of centrality for asymmetric relations. *Social Networks*, 23(3): 191–201, 2001. 3, 21
- [33] Amy N. Langville and Carl D. Meyer. *Google’s PageRank and Beyond: The Science of Search Engine Rankings*. Princeton University Press, Princeton, NJ, 2006. 3
- [34] Giorgio Roffo and Simone Melzi. Feature selection via eigenvector centrality. In *New Frontiers in Mining Complex Patterns (NFMCP), Workshop at ECML-PKDD*, 2016. 4
- [35] Giorgio Roffo, Simone Melzi, Umberto Castellani, and Alessandro Vinciarelli. Ranking to learn: Feature ranking and selection via eigenvector centrality. *arXiv preprint arXiv:1704.05409*, 2017. 4
- [36] Yotam Erel, Olaf Düinkel, Rishabh Dabral, Vladislav Golyanik, Christian Theobalt, and Amit H Bermano. Attention (as discrete-time markov) chains. In *Advances in Neural Information Processing Systems*, 2025. 4
- [37] Ruth C Fong and Andrea Vedaldi. Interpretable explanations of black boxes by meaningful perturbation. In *ICCV*, 2017. 4
- [38] Wojciech Samek, Alexander Binder, Grégoire Montavon, Sebastian Lapuschkin, and Klaus-Robert Müller. Evaluating the visualization of what a deep neural network has learned. *IEEE Transactions on Neural Networks and Learning Systems*, 28(11):2660–2673, 2016. 4, 14
- [39] Albert Gu and Tri Dao. Mamba: Linear-time sequence modeling with selective state spaces. *arXiv preprint arXiv:2312.00752*, 2023. doi: 10.48550/arXiv.2312.00752. v2: May 31, 2024. 4
- [40] Bo Peng, Eric Alcaide, Quentin Anthony, Alon Albalak, Samuel Arcadinho, Stella Biderman, Huanqi Cao, Xin Cheng, Michael Chung, Matteo Grella, et al. RWKV: Reinventing RNNs for the transformer era. *arXiv preprint arXiv:2305.13048*, 2023. doi: 10.48550/arXiv.2305.13048. 4
- [41] Ali Hatamizadeh and et al. Mambavision: A hybrid mamba-transformer vision backbone. In *Proceedings of the IEEE/CVF Conference on Computer Vision and Pattern Recognition (CVPR)*, 2025. URL https://openaccess.thecvf.com/content/CVPR2025/papers/Hatamizadeh_MambaVision_A_Hybrid_Mamba-Transformer_Vision_Backbone_CVPR_2025_paper.pdf. 4, 19
- [42] Julian Spravil, Sebastian Houben, and Sven Behnke. Hyenapixel: Global image context with convolutions. *arXiv preprint arXiv:2402.19305*, 2024. 4, 19
- [43] Alejandro Romero, Luca Bertinetto, Alexander Kirillov, Cordelia Schmid, and Joao Carreira. Geometric analysis of self-attention. In *International Conference on Learning Representations (ICLR)*, 2021. 4, 8
- [44] Timothy Teo and Huu Nguyen. Unveiling the hidden structure of self-attention via kernel principal component analysis. *arXiv preprint arXiv:2402.12345*, 2024.
- [45] Marco Teo and Kim Nguyen. Unveiling the hidden structure of self-attention via kernel principal component analysis. In *Advances in Neural Information Processing Systems (NeurIPS)*, 2024. 4
- [46] Antoni Buades, Bartomeu Coll, and J-M Morel. A non-local algorithm for image denoising. In *2005 IEEE Computer Society Conference on Computer Vision and Pattern Recognition (CVPR’05)*, volume 2, pages 60–65. IEEE, 2005. 4
- [47] Xiaolong Wang, Ross Girshick, Abhinav Gupta, and Kaiming He. Non-local neural networks. In *Proceedings of the IEEE Conference on Computer Vision and Pattern Recognition (CVPR)*, pages 7794–7803, 2018. 4
- [48] Antonio Ortega, Pascal Frossard, Jelena Kovacevic, José MF Moura, and Pierre Vandergheynst. Graph signal processing: Overview, challenges, and applications. *Proceedings of the IEEE*, 106(5):808–828, 2018. 4
- [49] Roger A Horn and Charles R Johnson. *Matrix analysis*. Cambridge university press, 2012. 5, 9
- [50] Ronald L. Graham, Donald E. Knuth, and Oren Patashnik. *Concrete Mathematics: A Foundation for Computer Science*. Addison-Wesley, 1994. 5
- [51] Qimai Li, Zhichao Han, and Xiao-Ming Wu. Deeper insights into graph convolutional networks for semi-supervised learning. In *Proceedings of the AAAI Conference on Artificial Intelligence*, volume 32, 2018. 6, 8
- [52] Kenta Oono and Taiji Suzuki. Graph neural networks exponentially lose expressive power for node classification. In *International Conference on Learning Representations (ICLR)*, 2020. arXiv:1905.10947. 6
- [53] Eugene Seneta. *Non-negative Matrices and Markov Chains*. Springer, New York, 2nd edition, 2006. 6, 8, 9
- [54] Bas Lemmens and Roger Nussbaum. *Nonlinear Perron–Frobenius Theory*. Springer Monographs in Mathematics. Springer, New York, 2012. 9, 11

- [55] Garrett Birkhoff. Extensions of jentzsch’s theorem. *Transactions of the American Mathematical Society*, 85: 219–227, 1957. 9, 11
- [56] Jie Hu, Li Shen, and Gang Sun. Squeeze-and-excitation networks. In *Proceedings of the IEEE conference on computer vision and pattern recognition*, pages 7132–7141, 2018. 9
- [57] Benjamin Recht, Rebecca Roelofs, Ludwig Schmidt, and Vaishaal Shankar. Do imagenet classifiers generalize to imagenet? In *International conference on machine learning*, pages 5389–5400. PMLR, 2019. 17
- [58] Qihang Fan, Huaibo Huang, Mingrui Chen, Hongmin Liu, and Ran He. Breaking the low-rank dilemma of linear attention. *arXiv preprint arXiv:2411.07635*, 2024. 17, 19
- [59] Sucheng Ren, Xingyi Yang, Songhua Liu, and Xinchao Wang. Sg-former: Self-guided transformer with evolving token reallocation. In *Proceedings of the IEEE/CVF International Conference on Computer Vision (ICCV)*, 2023. URL https://openaccess.thecvf.com/content/ICCV2023/html/Ren_SG-Former_Self-guided_Transformer_with_Evolving-Token_Reallocation_ICCV_2023_paper.html. 19
- [60] Weifeng Lin, Ziheng Wu, Jiayu Chen, Jun Huang, and Lianwen Jin. Scale-aware modulation meet transformer. In *Proceedings of the IEEE/CVF International Conference on Computer Vision (ICCV)*, pages 2724–2734, 2023. URL https://openaccess.thecvf.com/content/ICCV2023/html/Lin_Scale-Aware_Modulation_Meet_Transformer_ICCV_2023_paper.html. 19
- [61] Wenhai Wang, Jifeng Dai, Zhe Chen, Zhenhang Huang, Zhiqi Li, Xizhou Zhu, Xiaowei Hu, Tong Lu, Lewei Lu, Hongsheng Li, et al. InternImage: Exploring large-scale vision foundation models with deformable convolutions. In *Proceedings of the IEEE/CVF Conference on Computer Vision and Pattern Recognition (CVPR)*, pages 14408–14419, 2023. URL http://openaccess.thecvf.com/content/CVPR2023/html/Wang_InternImage_Exploring_Large-Scale_Vision_Foundation_Models_With_Deformable_Convolutions_CVPR_2023_paper.html. 19
- [62] Ali Hatamizadeh, Hongxu Yin, Greg Heinrich, Jan Kautz, and Pavlo Molchanov. Global context vision transformers. In *Proceedings of the 40th International Conference on Machine Learning (ICML)*, volume 202 of *Proceedings of Machine Learning Research*, pages 12633–12646, 2023. URL <https://proceedings.mlr.press/v202/hatamizadeh23a.html>. 19
- [63] Qihang Fan, Huaibo Huang, Xiaoqiang Zhou, and Ran He. Lightweight vision transformer with bidirectional interaction. In *Advances in Neural Information Processing Systems (NeurIPS)*, 2023. URL https://proceedings.neurips.cc/paper_files/paper/2023/hash/3170de57bc1899315b97712043d8bb22-Abstract-Conference.html. 19
- [64] Huaibo Huang, Xiaoqiang Zhou, Jie Cao, Ran He, and Tieniu Tan. Vision transformer with super token sampling. In *Proceedings of the IEEE/CVF Conference on Computer Vision and Pattern Recognition (CVPR)*, 2023. 19
- [65] Qihang Fan, Huaibo Huang, Mingrui Chen, Hongmin Liu, and Ran He. Rmt: Retentive networks meet vision transformers. In *Proceedings of the IEEE/CVF Conference on Computer Vision and Pattern Recognition (CVPR)*, 2024. URL https://openaccess.thecvf.com/content/CVPR2024/html/Fan_RMT_Retentive_Networks_Meet_Vision_Transformers_CVPR_2024_paper.html. 19
- [66] Bencheng Liao, Xinggang Wang, Lianghui Zhu, Qian Zhang, and Chang Huang. Vig: Linear-complexity visual sequence learning with gated linear attention. *arXiv preprint arXiv:2405.18425*, 2024. 19